2D Materials

PERSPECTIVE

Defects in hexagonal boron nitride for quantum technologies: a perspective

Tobias Vogl[1], Viktor Ivády[2,3], Isaac J Luxmoore[4] and Hannah L Stern[5,*]

[1] Department of Computer Engineering, TUM School of Computation, Information and Technology, Technical University of Munich, 80333 Munich, Germany
[2] Department of Physics of Complex Systems, Eötvös Loránd University, Egyetem tér 1-3, H-1053 Budapest, Hungary
[3] MTA–ELTE Lendület 'Momentum' NewQubit Research Group, Pázmány Péter, Sétány 1/A, 1117 Budapest, Hungary
[4] Department of Engineering, University of Exeter, Exeter EX4 4QF, United Kingdom
[5] Department of Materials, University of Oxford, Oxford OX1 3PH, United Kingdom
[*] Author to whom any correspondence should be addressed.

E-mail: hannah.stern@materials.ox.ac.uk

Keywords: solid-state defect, spin, quantum technologies, hexagonal boron nitride

OPEN ACCESS

RECEIVED
5 October 2025

REVISED
3 February 2026

ACCEPTED FOR PUBLICATION
24 March 2026

PUBLISHED
27 April 2026

Abstract

Atomic defects in solid-state materials are building blocks for future quantum technologies, such as quantum communication networks, computers, and sensors. Until recently, a handful of defects in a small selection of host materials have been possible candidates. Recent developments have revealed that hexagonal boron nitride, a wide-bandgap two-dimensional material, hosts single-photon-emitting atomic defects with access to optically addressable electronic and nuclear spins at room temperature. Now, atomically thin quantum devices that operate at ambient conditions are a possibility. In this perspective, we discuss the recent progress, and challenges, in understanding the fundamental photophysics of defects in hBN, as well as specific opportunities they present for the development of quantum technologies.

1. Introduction

A major challenge in the realisation of widespread quantum technologies is the development of material platforms where quantum states can be reliably accessed and controlled. A range of systems are being explored, including trapped atoms/ions, quantum dots, molecules and atomic scale impurities in solids, each with their own benefits and drawbacks [1]. Of these, it is impurities, or point defects, in solid-state materials that offer access to quantum coherent states at room temperature and are highly compatible with solid-state device engineering [2–4]. While point defects are ubiquitous to extended solids, it is isolated point defects in wide-bandgap host materials with quantised electronic transitions, at optical and microwave frequencies, that can be used to implement qubits. Single-photon emitting defects provide photonic qubits for quantum computing [5] and quantum communication protocols, such as quantum cryptography [6, 7]. Whereas defects with optically addressable electronic and nuclear spins fulfill many of the DiVicenzo criteria for quantum computing [8], and are building blocks for quantum sensors [9, 10], and repeaters and memories in quantum optical networks [3, 11].

Until recently, remarkably few defects in a small range of host materials have been intensively pursued for quantum information technologies. Most focus has been on diamond, where the large bandgap (5.5 eV) and spin-free carbon lattice provides a near-ideal host for defects. Research over decades on the negatively charged nitrogen vacancy centre (NV^-) [12] has resulted in numerous influential reports, including entanglement between an optical photon and the electronic spin of the defect [13], entanglement of the multiple electronic spins [14–16], quantum control over individual nuclear spins, extending to demonstration of multi-qubit quantum registers [17–19], and quantum microscopy using the spin of the NV^- centre as a nanoscale sensor [20–23]. These demonstrations have made defects important solid-state platforms for quantum applications. However, scalability is critical if lab-based demonstrations are to be translated to a new technologies. As such, focus is increasingly turning to the identification and development of defects in other materials, such as silicon carbide (SiC) [24, 25], silicon [26–29],

and galium nitride (GaN) [30], as these materials may offer easier defect integration to solid-state devices than diamond.

Over the past ten years, it has been discovered that hexagonal boron nitride (hBN), a wide-bandgap two-dimensional (2D) material, hosts optically- and spin-active defects [31–36]. Unlike 3D counterparts, hBN offers the potential for easier and more scalable integration to solid-state devices. Over the past 15 years the huge interest in 2D material electronics has meant the growth, transfer and device fabrication capabilities with hBN have become well established. hBN can be grown epitaxially at wafer scale, on a range of substrates, with well-controlled thickness (from monolayer to 100's nm) [37–41]. hBN can be transferred to a range of substrates and other (bulk and 2D materials) [42, 43], meaning that hBN layers can be integrated with on-chip optical components such as waveguides [44], cavities [45–47] and nanoantennas [48]. Moreover, electrical devices can be built around defect-active hBN layers to enable Stark tuning [49], charge control [50] and electrical excitation of defects [51].

These attractive capabilities are only relevant if hBN defects possess competitive magneto-optical properties. To date, defects in hBN show a mix of promising optical properties, even at room temperature, including high zero-phonon line (ZPL) fraction (as high as 0.8) [31, 52, 53], high brightness (MHz count rates) [54–56] and high single-photon purity [57]. Subclasses of optically active hBN defects possess optically addressable electronic and nuclear spins (on the ensemble and single-defect level) that can be coherently controlled, with microsecond coherence times at room temperature [33–36, 58–63]. These recent discoveries provide a platform to explore new defect physics and device engineering. However, research into hBN defects is still in its infancy and faces significant fundamental and practical challenges before it can be regarded as a competitive solid-state platform for quantum technologies. This perspective discusses the current progress and future challenges, experimental and theoretical, facing the next phase of development of hBN defects for optical and spin-based quantum technologies.

2. Quantum optical technologies

Single-photon-emitting defects are quantum light sources that provide a source of photonic qubits. An ideal on-demand single-photon-emitting defect emits strictly one photon at a time (single-photon purity) into a given spatiotemporal mode, with every emitted photon being identical (indistinguishable). Such systems are either required, or beneficial for, the development of quantum computing schemes, quantum simulation and quantum communication [32]. In this section we address the progress on applying hBN defects to two specific technologies of different levels of maturity: quantum key distribution (QKD) and quantum computing. QKD is a form of quantum communication where information is encoded in single photon states of light, which allows one to detect and quantify any eavesdropping attempt [64]. It is already a commercially available technology, however it currently typically uses attenuated classical light sources. The use of quantum light sources for QKD would enhance the secure data rate, but sources with high single-photon purity are strictly required. On the other hand, photonic quantum computing schemes utilise entanglement of single photons to perform logic gates and demands defects that can emit high rates of indistinguishable photons [5].

HBN presents a new material system to explore for both technologies. Defect emission has been observed in hBN ranging from the UV to near-IR, and covering the entire spectral range in between [31, 33, 65–69] (figure 1). With the exception of the negatively charged boron vacancy (V_B^-), the consensus is building that the majority of these defects are related to carbon substitutions in the hBN lattice, but differentiation of their atomic structures is still under intense theoretical and experimental investigation (see section 4). In this article, we broadly classify hBN defects by the energy of their ZPL (in section 3 by their spin signatures). Figure 1(a) shows the ZPL positions of different defects that emit across the UV–visible region. Important groups include the UV emitter (ZPL = 302 nm) [65, 74, 75], the B-centre (ZPL = 437 nm) [76, 77] and the emitters that span the green–red spectral region (ZPL = 550–700 nm) [31, 52, 69, 78], all of which are bright, single-photon emitters. For the green–red group, magnetic resonance studies indicate that multiple different atomic defects emit in this region (see section 3), while the UV and B-centres are associated with a single defect structure (proposed to be a carbon dimer [70] and carbon tetramer respectively [79]). In contrast, the V_B^- is a weakly emissive defect without an observable ZPL which is measured on the ensemble level, making it unsuitable for quantum information processing.

2.1. QKD

2.1.1. Single-photon purity

The ideal photon source for QKD is one that can produce high rates (>100 MHz) of high-purity single photons ideally at ambient conditions, a combination of properties that have so far have only been demonstrated by self-assembled quantum dots at cryogenic temperatures. A high single-photon purity means a high quantum efficiency (QE) combined

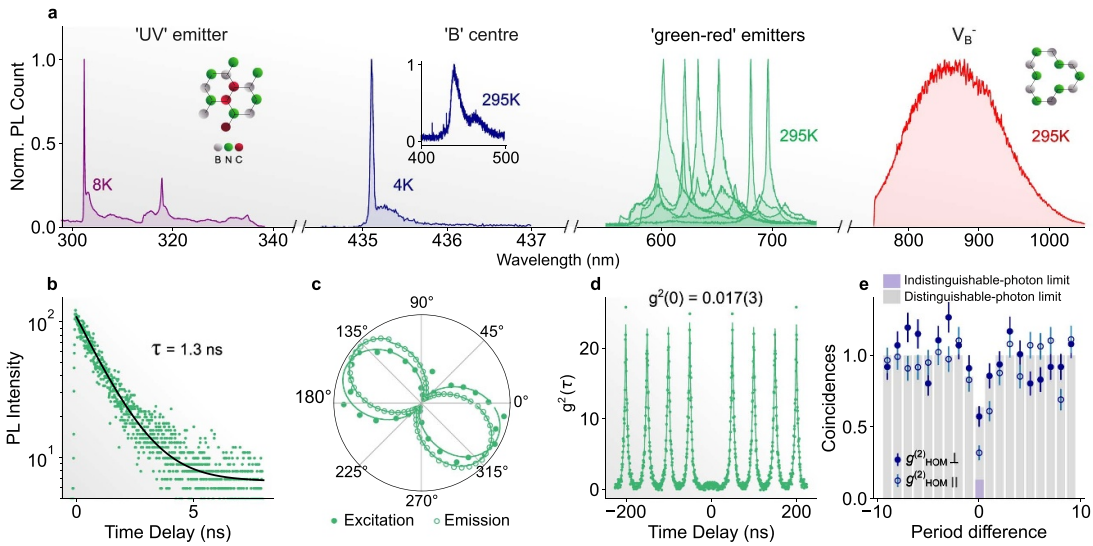

Figure 1. Optical properties of hBN defects. (a) Integrated photoluminescence (PL) spectra for different classes of hBN defects including the C_BC_N 'UV emitter' (purple trace, 8 (K) (reproduced from [70]. CC BY 4.0), the 'B' centre (4 (K) (blue traces, inset shows 295 (K) (reproduced from [71]. CC BY 4.0), 'green–red' emitting defects (green traces, 295 (K) (adapted with permission from [66]. Copyright (2016) American Chemical Society), and the V_B^- (red trace, 295 (K) (reproduced from [72]. CC BY 4.0). (b) Time-resolved PL of a 'green–red' emitting hBN defect. Adapted with permission from [46]. Copyright (2019) American Chemical Society. (c) Polarisation of excitation (bold circles) and emission (open circles) of hBN green–red defects. Reproduced from [57]. CC BY 4.0. (d) Second-order intensity correlation measurement ($g^{(2)}(t)$) of a 'green–red' hBN defect, displaying a $g^{(2)}(0)$ of 0.017(3). Reproduced from [57]. CC BY 4.0. (e) Two-photon coincidences from a Hong–Ou–Mandel measurement of a B-centre. The orange (blue) dots denote the normalised coincidence rate for the parallel-polarisation (orthogonal-polarisation) configuration of the input ports of the second beam splitter. The center peak provides the values of $g^{(2)}_{\mathrm{HOM}}(0) = 0.32 \pm 0.05$ (parallel case) and $g^{(2)}_{\mathrm{HOM}}(0) = 0.58 \pm 0.07$ (orthogonal case). The light-gray bars mark the theoretical values for distinguishable photons of $g^{(2)}(0) = 0.14$. The purple bar indicates the theoretical value for fully indistinguishable photons of $g^{(2)}(0) = 0.14$. Reprinted figure with permission from [73], Copyright (2023) by the American Physical Society.

with a low multi-photon probability (i.e. a high overlap with the single photon Fock state). The overall QE of a defect is determined both by the internal QE and the ease of photon out-coupling, a challenge for defects in high-refractive index materials. For the green–red hBN defects, the sub-ns to ns PL lifetimes translate to >GHz photon emission rates, as shown by the time-resolved PL decay of a green–red hBN defect in figure 1(b). In addition, the internal QE can reach 40%–80% [46, 77, 80] and photon out-coupling and collection can approach 100% due to the relatively low refractive index combined with the in-plane dipole of defects. Figure 1(c) shows the excitation and emission polarisation of a green–red defect [57].

The multi-photon emission probability of a defect is determined via second-order intensity correlation measurement, or $g^{(2)}(t)$. The reported $g^{(2)}(0)$ values for hBN defects vary significantly [31, 54, 81]. This may be affected by the wide range of setups and background correction methods used to conduct this experiment, as well as how clean the sample is in terms of background emission (noise). Notably, $g^{(2)}(0)$ of <0.015 have been reported across for the green–red emitters [54, 82] and polarisation-resolved measurements have improved $g^{(2)}(0)$ down to < 0.02 into free space at room temperature and without any background correction, as shown in figure 1(d) [57].

2.1.2. System efficiency

QKD is currently almost exclusively performed using weak laser pulses, as they can be generated with a low technical complexity and with low cost. The most efficient protocols use weak laser pulses with a varying intensity in so-called decoy protocols [83]. To be competitive with decoy protocols, the system efficiency of a quantum emitter (the probability that a photon is generated into the mode of the collection optics when a photon emission is triggered) should be similar to the mean photon number in the decoy protocol, typically around 0.4–0.5 [84]. To achieve this with defect systems, high QE, low internal optical losses and low $g^{(2)}(0)$ values ($g^{(2)}(0) < 10^{-2}$) are required. Initial demonstrations of QKD with green–red emitting hBN defects show lower secret key rate (the ultimate performance metric in QKD) of the hBN system compared to state-of-the-art laser-based systems [85, 86]. However, the QE, emission mode directionality and $g^{(2)}(0)$ for hBN defects can be improved via resonant cavity systems such that a system efficiency of the single-photon source exceeds 50% [46, 87, 88]. Problematic, even for a cavity-enhanced system is if the non-radiative decay happens via a pathway with a long-lived dark state. In this case, the singe photon source (and therefore the QKD system) would be out-of-operation for that time and not generate any signal. Further QKD demonstrations

should implement improved optical cavities [46] and cleaner crystals with less scattering [87], both of which are feasible to enhance the QKD performance. Numerical simulations have shown that the optical properties of cavity-coupled hBN emitters is theoretically sufficient to outperform laser-based protocols on short and medium distances (low-medium loss channels), e.g. up to 1000 km in a space-to-ground quantum channel, while the latter become more efficient for very long distances (high loss) [46, 89] if one assumes similar link parameters taken from the Micius mission [90] (i.e. a repetition rate of 100 MHz, a 30 cm telescope on the satellite, a 100 cm telescope in the ground station, standard atmospheric transmission, and a detection efficiency of 50%). A repetition rate of 100 MHz is compatible for most of the hBN defects, as their excited state lifetime is shorter than 10 ns.

Despite relatively few reports of microcavity-enhanced demonstrations with hBN single-photon emitting defects (small Purcell factors 1–4) [46, 87], the 2D host provides advantages for cavity coupling over defects in 3D crystals. Specifically, the in-plane dipole simplifies the alignment with rotation symmetric cavities and 2D material transfer should be beneficial for cavity fabrication.

2.1.3. Emission wavelength

Besides these fundamental requirements on the single-photon emitter for QKD, the mode of photon propagation, and thus photon wavelength, are also important considerations. Photons can be transported in QKD protocols via existing optical fibre infrastructure or via free-space. For fiber-based channels, the photon wavelength should be within the telecom C-band (1550 nm) or in the O-band (1330 nm) to minimise transmission losses. This presents a potential restriction for hBN as a platform, as so far most known hBN optical defects emit in the visible region. It has been predicted using density functional theory (DFT) calculations that certain hBN defects should emit in the O-band (e.g. O_NS_N [91]) and C-band (e.g. Al_NAl_N, $In_NN_BV_N^{-1}$ and $P_BV_B^{-1}$ [92]). Further DFT studies suggested that Stark tuning defects could also be used to shift the emission into the NIR region [93]. It should be noted that DFT calculations usually assume a temperature of 0 K. As the temperature increases, the band gap decreases which usually shifts the defect levels and therefore also the energy gap between two states. For emitters where the transition energy is low (such as in the C-band) this can be significant when comparing room temperature emission spectra to DFT calculations. In addition, DFT has only finite accuracy, which is difficult to benchmark, therefore, small transition energies should generally be treated with care. Experimentally, there has been no demonstration of any hBN emitter in the O- or C-band yet. The lack of experimentally observed telecom emitters could so be due to the fact that most research groups have PL setups designed for visible wavelengths and therefore cannot detect any NIR light. The same challenge applies to other host materials which is why there are few reports of defect emitters in the O- [26, 94, 95] and C-band [96]. Future work with setups that are designed to detect NIR photons, combined with ion implantation to create defects, should be performed to identify new defects compatible with the telecom C-band. Once these emitters have been fabricated, the direct fiber integration has potential to be straightforward due to the 2D geometry [97].

QKD can also be carried out via free space [90, 98]. In this case, any transmission window of the atmosphere can be used. Due to the broad emission range of hBN defects, there are many emission wavelengths of hBN coinciding with an atmospheric transmission window. Free-space QKD typically uses photon polarisation as the quantum encoding mechanism, which makes it directly compatible with the linear polarisation of hBN defects without any loss (which would occur if one has to polarise unpolarised light). Unfortunately this requires fast polarisation modulators which are not commercially available. This has provided the key limitation to the speed of QKD experiments with green–red emitting hBN defects (with modulator speeds of 1 MHz [85] and 500 kHz [86]), where the short excited lifetime on the order of 300 ps [99] to 3 ns [31] in theory allows for lifetime-limited repetition rates well exceeding 100 MHz. Routes forward should either include faster modulation schemes or the spatial overlap of differently polarised hBN defects that are identical in all other degrees of freedom (spectral shape, lifetime, etc) [100].

Despite the apparent challenges to deliver free-space QKD, hBN quantum emitters (green–red) have been proposed for daylight QKD schemes [89] and have been qualified for use in space applications [101], which allows one to use them as quantum light sources for satellite-based QKD [102]. Success of this daylight QKD scheme will rely on future demonstrations of strain or Stark tunability of the emission wavelength, as specific wavelengths have to be matched within the fraction of a nanometre. Such precise tuning would also allow one to have multiple sources operating at slightly offset emission wavelengths which enables multiplexing and therefore enhances the QKD data rates. To date, several promising demonstrations of such ZPL tuning have been reported. For the green–red emitters, room temperature tuning via Stark (a fraction of an meV) [49] and strain tuning (several meV) [54]. At low temperature, Stark tuning has demonstrated tunability of several GHz, for the B-centre [103]. In addition, for satellite-based QKD, fast on-demand excitation (that can out-compete the excited state lifetime to prevent re-excitation during one pulse) will be needed to maintain a very low $g^{(2)}(0)$, which is

not easy on a satellite. To address this, one can imagine fast and compact, integrated electrical excitation schemes with hBN defects embedded in heterostructure devices, which are currently under development [104, 105], but with far inferior optical properties compared to optically excited emitters. The reason for this is that with electrical excitation one typically cannot isolate the excitation well enough as compared to a tightly focused laser, which results in a poor photon purity as basically every defect in the heterojunction area is excited simultaneously. Moreover, this excitation is also not as efficient compared to the high intensity of a focused laser, which results in a poor QE. Due to the insulating nature, this generally only works with very thin hBN, so the challenge is to maintain a high photostability of the emitters despite the thin host crystal.

2.2. Optical quantum computing

2.2.1. Indistinguishable photons

To realise any quantum computer, a universal set of gates (into which any algorithm can be decomposed into) is required. As photons do not directly interact with each other, deterministic two-qubit gates (such as the CNOT gate) cannot be realised directly with linear optics [106]. The solutions are either probabilistic gates (which are not scalable), some non-linear interaction medium (which are usually not very efficient), or one-way quantum computing protocols (which requires the generation of highly entangled cluster states [107]). These states can be generated from single photons if they are indistinguishable. Indistinguishability here means a high two-photon interference contrast. The number of qubits that can be entangled efficiently scales with this visibility and values exceeding 99% are required to achieve fault-tolerant quantum computing [107]. Two-photon interference has been demonstrated for B-centre defects in hBN, even though the experiment was done at cryogenic temperatures (4 K) and a partial visibility of 0.44(11) (i.e. lower than the ideal value of 1) was achieved [73] (figure 1(e)). Generally, there have been few reports of optical linewidths approaching the lifetime limit for hBN defects. At room temperature it is hardly imaginable to achieve visibility $>$ 99% with the visible hBN single-photon emitters without addressing the mechanisms that give rise to linewidth broadening [108]. To date, reports have indicated charge-related spectral wandering and phonon coupling play a dominant roles in optical broadening for hBN defects [50, 52, 108, 109]. It is reported that mechanical decoupling from phonons can result in Fourier transform-limited linewidths below 100 MHz at room temperature [110, 111]. It should be mentioned that this has only been reported for a specific defect type (speculated to be an interlayer defect) and as of yet has not been observed for other hBN defects. Moreover, this results in an in-plane emission directionality, which is then difficult to collect with a high efficiency.

Cavity funneling (i.e. forcing the emitter to emit into the resonnant mode by blocking any off-resonant excitation) can be used to enhance the indistinguishability and directionality simultaneously [112], but this requires a cavity linewidth on the order of 100 MHz to achieve a visibility of 90% [46]. A large free spectral range of the cavity is required to block any phonon modes (which means one cannot simply make the cavity longer to reduce the linewidth). Otherwise, one would sample the free space emission spectrum at the free spectral range and only photons from the same peak are indistinguishable and one has to filter out other peaks. This in turn results in a low efficiency (or photon rate) of the single-photon source. This is the reason why there has been no demonstration of quantum computing with hBN, though there have been collective measurements on single qubits performed on single photons from hBN [113]. Future work should therefore focus on the realisation of indistiguishable single photons and the generation of cluster states for optical quantum computing.

3. Spin-based quantum technologies

3.1. Spin-active hBN defects

Defects with optically addressable electronic and nuclear spins are attractive systems for spin-based quantum technologies, such as repeaters for optical networking and quantum sensors [3]. hexagonal Boron Nitride represents the first 2D material platform where optically addressable spin defects have been identified at room temperature. Since 2020, multiple classes of hBN spin defects have emerged. Figure 2 presents the different spin-active hBN defects, while table 1 compares their spin properties. To date, the most studied is the V_B^- [33, 58, 60], which is a radiative ground state spin triplet ($S = 1$) system. In the absence of hyperfine coupling, $S = 1$ spin systems are described by a Hamiltonian of the type:

$$H = H_{ZF} + H_{ZE}, \tag{1}$$

$$H_{ZF} = DS_z^2 + E\left(S_x^2 - S_y^2\right), \tag{2}$$

$$H_{Ze} = \frac{\gamma_e}{2\pi}\mathbf{B}\cdot\mathbf{S}, \tag{3}$$

where H_{ZF} is the zero-field splitting (ZFS) term, H_{ZE} is the Zeeman term, D and E are the longitudinal and transverse ZFS parameters respectively that define the defect's x, y, z principal axes in units of Hz, $\mathbf{S}$ is the $S = 1$ operator with cartesian components $S_{x,y,z}$, γ_e is the electron gyromagnetic ratio and $\mathbf{B}$ is the applied magnetic field. For the V_B^- the ground- and excited-state D are $\sim$3.5 GHz [33] and $\sim$2.1 GHz [122], respectively, and the spin

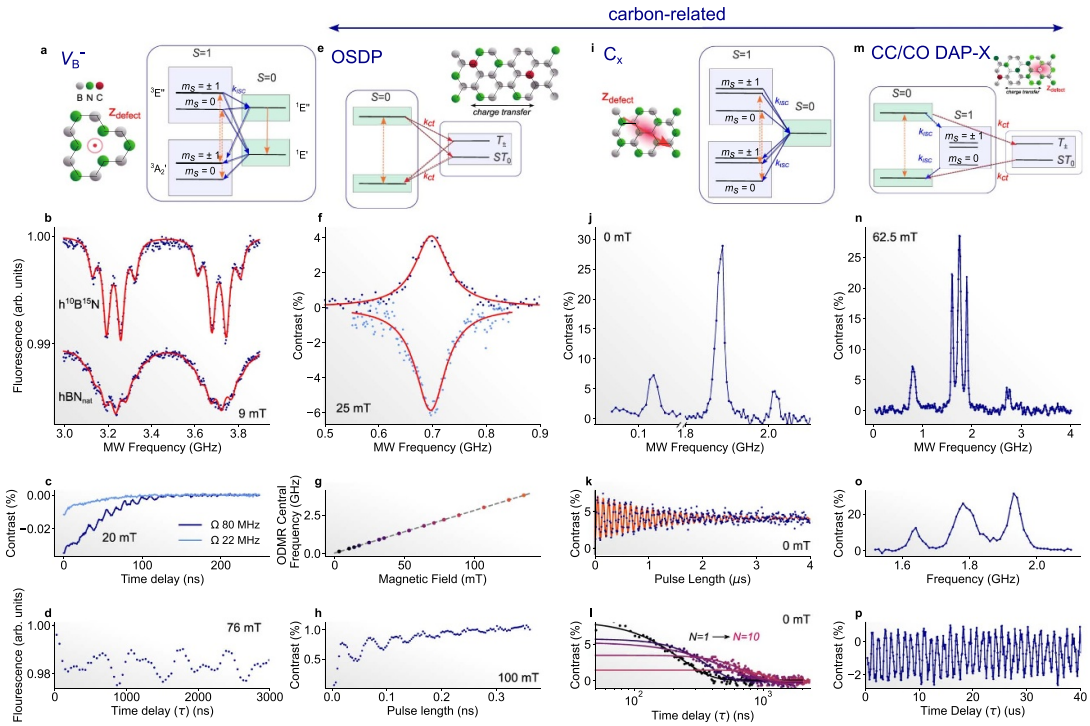

Figure 2. hBN spin defects. (a) Right: The simplified electronic structure of the V_B^- defect, reproduced from [60]. CC BY 4.0. The orange arrows represent optical excitation/emission between ground and excited states, and blue arrows represent intersystem crossing. Left: A schematic of the V_B^- defect, where z_{defect} indicates an out-of-plane quantisation axis. (b) Measured ODMR spectra of V_B^- in $h^{10}B^{15}N$ and naturally abundant hBN_{nat} at magnetic field $B_z \sim 9$ mT. Solid lines represent multi-peak Lorentzian fits, reproduced from [61]. CC BY 4.0. (c) Comparison of spin echo for V_B^- ensembles at low (22 MHz, black) and high (80 MHz, red) Rabi frequency, Ω. At high Rabi frequency, the contrast is stronger since a higher proportion of spins are controlled, reproduced from [72]. CC BY 4.0. (d) Measurement of ^{15}N nuclear spin Rabi oscillations for the V_B^-, reproduced from [61]. CC BY 4.0. (e) An 'optical spin defect pair' (OSDP) model used to explain the presence of $S = 1/2$-like ODMR signatures that are measured across different hBN materials. Orange arrows represent optical excitation/emission between ground and excited states and red dashed arrows represent charge transfer. The electronic model is modified from [114]. The upper part of the figure shows a potential atomic structures for a OSDP, where charge transfer occurs between two separate defects. (f) ODMR spectra for two single defects in carbon-doped multilayer hBN, measured with an applied field of 25 mT, reproduced from [35]. CC BY 4.0. (g) The central resonance frequency for a single carbon-related defect in carbon-doped multilayer hBN, reproduced from [35]. CC BY 4.0. (h) Rabi oscillations measured for ensembles of carbon-related defects in an exfoliated single-crystal hBN flake, at B = 100 mT. The resonance frequency being driven is 2.9 GHz. Reproduced with permission from [62]. CC BY-NC 4.0. (i) The proposed electronic structure for C_x, a carbon-related $S = 1$ defect in hBN with $D = 1.97$ GHz and $E = 60$ MHz. The optical spin polarisation mechanism includes spin-dependent intersystem crossing (blue arrows) via a single metastable state. The orange arrows represent optical excitation/emission. The left hand image represents the in-plane quantisation axis for the defect, of unknown atomic structure. (j) cw-ODMR spectra for a single C_x defect. (k) Rabi oscillations for C_x defect, fit to a function of the form $\exp(-t/T_{Rabi})\sin(2\pi t\Omega - \phi)$ (orange curve), where ϕ is the phase offset, Ω is the Rabi frequency and T_{Rabi} is the decay lifetime of the Rabi oscillations. Measured at 0 mT with drive frequency of 1.9 GHz. (l) Dynamic decoupling measurements with Nπ refocusing pulses, where each measurement is fit to $\exp[-(t/T_{DD})^{\alpha}]$. (j)–(l) are reproduced from [36]. CC BY 4.0. (m) The proposed electronic structure of a $S = 1$ carbon related defect formed in exfoliated hBN via CO_2 implantation and thermal annealing. This defect type shows both $S = 1$ and $S = 1/2$ like signatures and has been assigned to a pair of spin defects ($S = 1/2$ and $S = 1$) where the optical spin polarisation mechanism includes both spin-dependent intersystem crossing and charge transfer. One of the defects of the pair is predicted to be a C–C or C–O donor acceptor pair (DAP). Schematic modified from [63]. The schematic shows a possible atomic structure for the two defects of the pair, where one has an out-of-plane quantisation axis in its triplet state. (n) An ODMR spectrum of one of the defects of this category, measured with an out of plane magnetic field of 62.5 mT. (o) The ODMR spectrum after nuclear spin initialisation revealing polarisation of the ^{15}N nuclear spin. (p) An example of nuclear spin Rabi oscillation, persisting for 40 μs without significant decay. (n)–(p) are reproduced from [63]. CC BY 4.0. All data were measured at 295 K.

quantisation (z) axis is out-of-plane, represented by the schematic in figure 2(a). Similar to the NV^- centre, spin-initialisation is achieved through optical pumping. The optically detected magnetic resonance (ODMR) spectra of the V_B^- reveal hyperfine coupling to the nearest three nitrogen nuclei, as shown in figure 2(b). The room temperature spin relaxation (T_1) and Hahn Echo spin coherence (T_2^{echo}) timescales are of the order of 10 μs [58] and 100 ns, respectively (figure 2(c)) [33, 72, 123].

The V_B^- has a low QE due to nanosecond forward intersystem crossing [60], combined with a slow radiative decay, predicted to be ∼10 μs [124], but not yet measured experimentally. This has prevented optically addressing single defects, despite attempts using nanocavities [125, 126]. The reverse intersystem crossing has recently been reported to be around 10 ns [127], much shorter than theoretical predictions [124], but which explains why PL can be measured despite the low QE of the triplet state.

Table 1. Spin-active hBN defects. Comparison of the hBN spin defects with the NV^- centre. ZPL = Zero Phonon Line. *D* and *E* are the zero field splitting parameters. The electronic spin coherence is reported for room temperature (RT) measurements. *E–N* coupling refers to electro-nuclear coupling.

Defect	ZPL (nm)	*D*, *E* (GHz)	Electronic spin coherence (RT)	T_1 (μs) (RT)	*E–N* coupling	Nuclear spin coherence	References
V_B^-	750–1000	3.48, 0.06	$T_2^* = 50$ ns, $T_2^{echo} = <100$ ns, $T_2^{DD} = 4$ μs ($N = 1000$)	10	Yes	$T_2^* = 3.5$ μs	[33, 58, 60, 72, 115]
OSDP	400–800	<50 MHz	—	10–15	No	—	[34, 35, 56, 62, 116, 117]
C_x	590(15)	1.971(25), 62(10)	$T_2^* = 106(12)$ ns, $T_2^{echo} = 228(11)$ ns, $T_2^{DD} = 1.08(4)$ μs ($N = 10$)	30–200	No	—	[36, 118]
$C_B^+ C_N^0$-DAP-X	570–700	~1, 0.1–0.4	$T_2^{echo} = 100$–200 ns, $T_2^{DD} = 38$ μs ($N = 1024$)	17–216	Yes	$T_2^* = 16.6$ μs, $T_2^{echo} = 162$ μs	[63, 119]
NV^-	637	2.88, <1 MHz	$T_2^{DD} = 3.3$ ms ($N = 295$)	6000	Yes	$T_2^* = 1.9$ min	[12, 120, 121]

Control of single electronic spins in hBN has been demonstrated with defects that emit in the green–red spectral range, suspected carbon-related defects [34–36, 63, 78]. Curiously, a range of different ODMR signatures have been observed for defects that emit in this region, meaning the ODMR itself provides currently the best tool to distinguish between them. Figures 2(e)–(p) presents the ODMR of the suspected carbon-related hBN defects. In general, three different species have been observed. The first show no appreciable ZFS [34, 35] (figures 2(e)–(h)). For these defects, the ODMR is characterised by a central ODMR frequency that follows a g-factor of ∼2 (figure 2(g)), a broad linewidth without clear hyperfine structure, and ODMR contrast that can be positive or negative (figure 2(f)). Coherent control of these spins is difficult [62] (figure 2(h)) and T_1 is ∼10–15 μs [34, 35, 56, 62]. ODMR spectra fitting this description have now been observed for wide range of carbon-doped hBN samples [114] on both the ensemble and single defect level, and, in some cases, co-existing with $S = 1$ signatures on a single defect [34, 35, 56, 62, 63, 78, 116]. Recently, a model invoking charge transfer between a pair of separate spin defects (dubbed the OSDP model) in the 2D lattice has been proposed to explain these findings [62, 116]. In this model, charge transfer from an optically excited $S = 0$ defect to a nearby dark $S = 0$ defect produces two weakly coupled $S = 1/2$ defects that can give rise to an ODMR-active metastable state, in a similar way to radical pair molecular systems [128]. Figure 2(e) presents the proposed electronic structure for this defect type and a schematic of its atomic structure. This proposed charge transfer mechanism would explain the wide spread of emission wavelengths associated with some defects that show the '$S-1/2$'-like ODMR signatures. If correct, the prevalence of spin pairs in hBN that can give rise to ODMR reveals a unique system where spatial proximity between defects may be engineered to tune ODMR properties, such a ZFS parameters or ODMR contrast.

The other two groups are strongly coupled $S = 1$ systems with GHz ZFS [36, 63]. These systems are represented by figures 2(i)–(p). The first reported, denoted C_x in this article, possess a $S = 1$ ground state with $D \sim 1.97$ GHz and $E \sim 60$ MHz, an in-plane spin quantisation axis and high (up to 90% reported) ODMR contrast [36, 118]. This defect is formed in metal organic vapour phase epitaxy (MOVPE)-grown hBN multilayers in the presence of a carbon-based precursor (triethyl boron) [38]. Figure 2(i) shows the electronic structure of this defect and schematic of the atomic structure, depicting the in-plane spin quantisation axis. Figure 2(j) is the cw-ODMR spectrum and figure 2(k) presents the rabi oscillations measured for this defect, both at 0 mT and room temperature. The narrow and consistent distribution of ZFS parameters measured for this defect indicate a specific atomic structure. Efficient coherent spin control is possible at zero magnetic field, with $T_1 \sim 100$'s of μs and $T_2^{\text{echo}} \sim 200$ ns that can be extended beyond a microsecond via decoupling pulse protocols [36] (figures 2(k) and (l)).

Distinct, single carbon-related defects with strongly coupled $S = 1$ signatures and an out-of-plane quantisation axis have recently been reported [63, 129] (figures 2(m)–(p)). These signatures are observed in hBN crystals that have been irradiated with $^{13}CO_2$ and annealed. The ODMR reveals a spin with $D \sim 1$ GHz and $E \sim 100$–400 MHz with similar electronic spin coherence properties as C_x. The $S = 1$ ODMR resonances are typically accompanied by an $S = 1/2$ ODMR resonance, which reveals clear hyperfine coupling of 100–300 MHz, associated with coupling to a neighbouring ^{13}C nuclear spin, as shown in the cw-ODMR spectrum presented in figure 2(n). The coexistence of both $S = 1$ and $S = 1/2$ signatures on the same defect suggests the presence of ODMR is due to both intersystem crossing and charge transfer processes (proposed to be the OSDP mechanism) that take place on the same defect (figure 2(m)) [63]. The $S = 1/2$ ODMR lines are assigned to a carbon DAP ($C_B^+C_N^0$-DAP-2) or carbon-oxygen complex (C_BO_N), while the identity of the structure giving rise to the $S = 1$ signatures is unknown at this stage, hence we denote this defect type CC/CO DAP-X [63].

Many of these spin hBN defects have been observed for the first time in the last couple of years. There is much work left to do to establish their full photophysical properties, atomic structure and reproducible fabrication processes. In the following sections we highlight opportunities presented by these spin defects for various spin-based quantum technologies.

3.2. Optical networks

Future global optical quantum networks will consist of a distribution of quantum states and entanglement to deliver secure global quantum communication, connectivity of quantum devices, and potentially a quantum internet [11, 130]. In such a network, quantum information and entanglement will be distributed across a web of nodes via photons [3, 11]. Each node will be composed of a physical system (the quantum repeater) that can send and retrieve quantum photonic information and store it in a long-lived quantum memory (typically spin states). Quantum repeaters based on solid-state defects with optically addressable spins have been explored theoretically [131] and experimentally [16, 132]. In the majority of these schemes, entanglement of distance spins is achieved via optical quantum erasure measurements which removes the which-path information on the origin of the photon.

To act as a repeater, a defect must have excellent optical properties, namely efficient and coherent optical transitions that are spin-dependent and spectrally resolvable [3, 131, 133]. On the spin side, the electronic spin must couple coherently to emitted photons, as well as to neighbouring nuclear spins so the defect can store quantum information while simultaneously setting up a new photonic link. This multi-qubit quantum register of electronic and nuclear spins can facilitate distributed entanglement over $>$ than 2 nodes, as demonstrated for the NV^- centre [16]. In terms of the spin coherence timescales, the electronic spin T_2 must be long enough long enough for propagation of the photon to the next node to establish entanglement [134, 135]. Practically, this mean the single- and two- gate timescales, entanglement efficiency and photon propagation time all set the minimum feasible timescale for T_2 [135]. Recently, it has been shown that electronic spin coherence times of 100's μs are not prohibitive for long-distance (10's km) entanglement, provided coupling to longer-lived nuclear spins is present [136].

The strongly coupled $S = 1$ hBN defects (C_x and CC/CO DAP-X) present the first feasible 2D spin systems to explore for quantum repeaters. Both show single qubit gates times of 10's ns and the potential for reasonable optical efficiency, however the spin coherence timescales are far shorter than for the NV^- centre. Major spin-challenges include overcoming the dense nuclear spin bath and access to individual nuclear spins that can provide quantum memories.

3.2.1. Mitigating spin decoherence

A challenge for all hBN spin defects is mitigating the magnetic noise from the spin-rich BN lattice, which is the main contributor to spin decoherence [137, 138]. Standard approaches for reducing nuclear spin noise in other defect systems include isotopic purification [25, 139] and dynamical decoupling protocols [140]. Removal of nuclear spins altogether is not possible in hBN (all B and N isotopes are spin active), but decoupling the electronic and nuclear spins has been demonstrated for both the V_B^- [72, 141], single C_x defects [36] and, very recently, the CC/CO DAP-X defects [119]. To date, these efforts have extended the electronic spin coherence to $\sim$50 μs, achieved at room temperature. These timescales are shorter (2–3 orders of magnitude) than can be achieved in diamond [120] and silicon carbide [142]. Experimental and theoretical studies of V_B^- have, to date, provided the most insight to spin decoherence mechanisms in hBN [33, 58, 138]. At low magnetic field, cluster correlation expansion modeling methods have indicated that short-range hyperfine interactions with the neighbouring ^{14}N, as well as nuclear spin-nuclear spin flip-flops drive decoherence [123, 138]. Enrichment of the host hBN with ^{10}B has been theoretically and experimentally confirmed to extend the coherence time from $\sim$90 ns to $\sim$190 ns [61]. This is because the reduced gyromagnetic ratio of ^{10}B over the naturally more abundant ^{11}B results in a weaker hyperfine interaction and boron nuclear spin flip-flop rates [123].

At fields as strong as a few Tesla, the coherence time T_2^{echo} extends to 36 μs [143] in agreement with theoretical predictions [138, 144]. In this high-field regime decoherence is dominated by dipole–dipole interaction-induced nuclear spin flip-flop interactions of homonuclear spin pairs [138]. Theoretical predictions show that magnetic dipolar coupling between the nuclear spins is partially suppressed in hBN via the nuclear quadrupole interaction [144].

A similar theoretical investigation of decoherence of the carbon-related single spin defects in hBN is not currently possible because their atomic structures are not yet confirmed. The decoherence mechanisms are likely to be qualitatively similar to those for V_B^-, however the different hyperfine interactions and defect symmetry will give rise to important quantitative differences, such as the field strengths required for changes in T_2. For example, for C_x the significant transverse ZFS (E) (related to the defects' symmetry), relative to the strongest hyperfine interaction, produces a clock transition at zero magnetic field [145] which decouples the electronic spin from the nuclear spin bath in a small region around zero magnetic field [36].

Detrimental spin noise can also be due to impurity electronic spins in the material. Cross relaxation between V_B^- and $S = 1/2$ impurities in the hBN lattice has been reported in several ODMR studies [62, 122]. Similar cross relaxation between bright and dark spin defects is likely to be prevalent in a range of carbon-doped hBN materials where the defect density is high, although there have been no detailed studies of this to date.

3.2.2. Coherent control of nuclear spins

Despite being a major of source of decoherence, strongly coupled nuclear spins can present an important resource for quantum networking applications. Individual nuclear spins that are strongly coupled (when the hyperfine coupling is greater than the dephasing rate ($1/T_2^*$)) to the central electronic spin can be individually initialised and controlled, enabling access to longer-lived quantum memory and multi-qubit entanglement [17, 146].

While there is an abundance of spin-active nuclei in hBN, the challenge is to identify individually strongly coupled candidates that can be controlled in isolation from the bath. This was first demonstrated in hBN with the V_B^- [115]. Here, polarisation of the three ^{14}N nuclei surrounding the V_B^- can be achieved at the excited/ground state level anti crossings (ESLAC/GSLAC) of the defect [115]. Using tailored pulse sequences to control both electronic and nuclear spins, spectroscopy of the ^{14}N nuclei revealed an effective nuclear-nuclear coupling

constant of 3.4 MHz at the GSLAC. Coherent control of the ^{14}N nuclei resulted in an inhomogeneous dephasing time (T_2^*) of 3.5 μs [115]. Dynamic nuclear polarisation of isotopically engineered h^{10}B^{15}N was more recently demonstrated, revealing improved resolution of the hyperfine coupling and coherent control of the ^{15}N nuclei [61] (figure 2(d)). While these demonstrations were the first examples of nuclear spin polarisation in a 2D material, the low QE of the V_B^- precludes the system from being applied to networking.

In a breakthrough result, single nuclear spin control has recently been demonstrated via single hBN spin defects [63]. This was demonstrated using the newly-identified carbon-related defect that is assigned to a DAP in the lattice which is coupled via charge transfer to a second defect (figures 2(m)–(p)). In this study, hyperfine coupling to a neighbouring ^{13}C nucleus is observed as a 300 MHz-splitting in the ODMR (figure 2(n)). Via optical polarisation and a SWAP gate to intialise the ^{13}C nuclear spin, coherent control revealed $T_1 = 144\ \mu$s, $T_2^* = 16.6\ \mu$s and $T_2^{\text{echo}} = 162\ \mu$s, setting a new record for nuclear spin coherence in the hBN system [63].

In general, the microsecond spin coherence timescales that can be accessed for the electronic spin of the hBN defects is not prohibitive for use in optical networking, as long as entanglement generation rates are faster [147]. For the hBN spins, microwave control of the spin is relatively slow (single qubit gate times typically 10–50 ns) which may present challenges for systems where this is long compared to T_2. More work is needed to determine the effect of magnetic field strength, isotopic composition, layer number, strain and defect density on the electronic spin coherence that can be achieved via decoupling approaches. For nuclear spin coherence, the timescales demonstrated so far (100's μs) are promising but still shorter than what can be accessed in diamond-based systems (typically seconds) [136]. Future work is required to determine the true limit to nuclear spin coherence, when this is not limited by the electronic T_1 [63].

3.3. Quantum sensing

Spin defects, namely NV$^-$ centres, are rapidly becoming established as an important quantum sensing platform for biomedical applications [148, 149] and materials characterisation [150]. Their spin states can be sensitive to small changes in magnetic field, as well as temperature, pressure, strain, stress and electric field. Combined with their atomic length scale, this enables mapping of these physical quantities with nanoscale spatial resolution. Meanwhile, their coherence properties and optical readout can enable unprecedented sensitivity.

Spin defect-based sensors utilise either a single defect or a large ensemble of defects as the active sensor. Ensemble-based sensing is typically performed in a widefield optical setup where the spatial resolution is diffraction limited, but where the use of many defects gives higher sensitivity (figure 3(a)). In contrast, the spatial resolution for single-defect sensors is fundamentally limited by the nanoscale spatial extent of the electronic wavefunction, but in practice by the defect-sample distance. Sensors employed for nanoscale sensing are typically scanned over a sample using an atomic force microscope. This sensing modality is most developed with NV$^-$ centres [21, 23, 151] where scanning probe magnetometers using single defects are now well developed and even commercially available [22, 150, 152–156].

While hBN defects are unlikely to compete with NV-based sensors with regards to spin coherence time, they display other advantages that may make them competitive sensors for particular applications. The atomically-thin nature of the hBN host material presents opportunities for nanoscale sensing and imaging with nm-spatial resolution [10]. Meanwhile, the ability to easily integrate hBN layers with other materials opens doors to *in-situ* imaging of 2D devices. Like diamond, hBN is also bio-compatible [159], and early results show the defects have high susceptibility to a range of physical factors which could see the defects being useful probes in biological context. Many of these areas are under rapid investigation and it is likely that quantum sensing will be the first area where hBN defects are industrially applied.

3.3.1. Wide-field quantum sensing

Progress towards applications with V_B^- ensembles has been rapid, with proof of concept experiments exploring their use in temperature [160, 161], pressure [162] and strain [163, 164] sensing, and particularly in wide-field magnetometry [157, 165, 166]. V_B^- ensembles have been integrated with ferromagnetic materials for *in-situ* magnetometry, for example in sensing the DC stray field from 2D ferromagnets [157, 165, 167], spin noise relaxometry [167, 168] and sensing spin waves [166, 168, 169]. Figure 3(b) presents a stray magnetic field map of $CrTe^2$ measured using the boron vacancy defects. To date, the best reported DC-magnetic field sensitivity is on the order of $\mu\text{T}\sqrt{\text{Hz}}^{-1}$ [170], inferior to the state of the art for ensemble NV$^-$ centre sensors (nT $\sqrt{\text{Hz}}^{-1}$) [171]. However, this is partly explained by the fact that the sensitivity scales with the square root of the number of defects in the ensemble [156], and much larger sample volumes are typically used in the NV$^-$ centre experiments. Whilst this can be addressed in future, the spin coherence time and QE are also superior for NV$^-$ centres, and it may be difficult for V_B^- ensembles to directly compete purely in terms of sensitivity in DC magnetometry.

In the case of AC magnetometry, dynamic decoupling pulse sequences can be implemented to

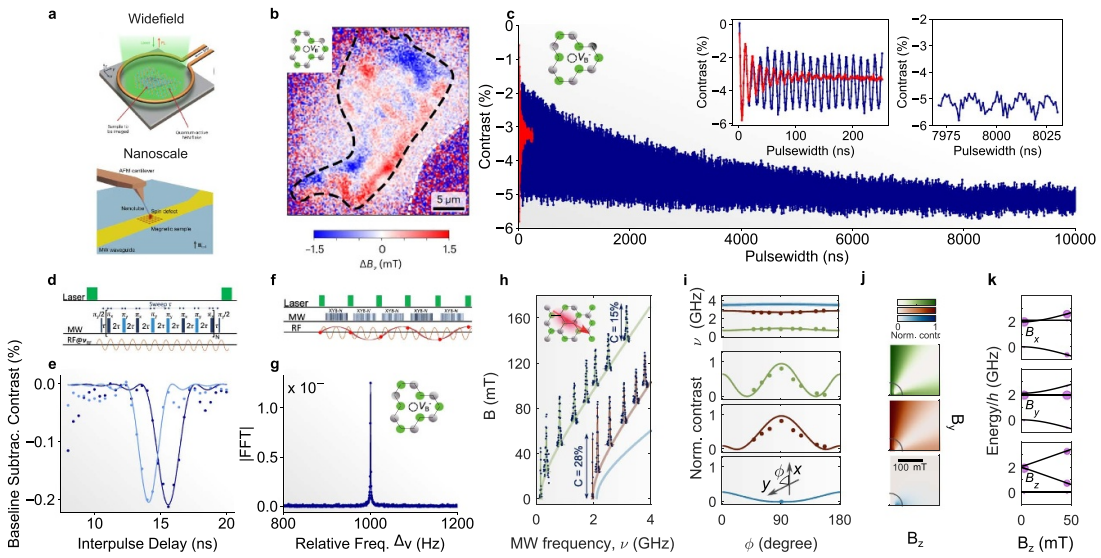

Figure 3. Quantum sensing with hBN defects. (a) Schematic of widefield and nanoscale quantum sensing. Adapted from [157], with permission from Springer Nature. Reproduced with permission from [158]. CC BY-NC 4.0. (b) Magnetic field map of a $CrTe_2$ flake, imaged using the V_B^-, adapted from [157], with permission from Springer Nature. (c) Comparison of unprotected Rabi oscillation (red trace) and amplitude modulated CCD scheme, for the V_B^- (blue trace), showing stabilisation of Rabi oscillation on μs-timescale. Inset figures show zoomed regions of the Rabi oscillations. Reproduced from [72]. CC BY 4.0. (d) Pulsed dynamical decoupling protocol used for sensing RF signals (V_B^-). (e) Response of the V_B^- sensor as fluorescence contrast dips occurring at matching of the interpulse delay (τ) with the RF signal period according to: $\tau = 1/(4\nu_{RF})$. The data points (dots) are best fitted with a $(\text{sinc})^2$ function. (f) Coherently Averaged Synchronized Readout (CASR) protocol. XY8-2 subsequences are synchronized to the sensing frequency for 2 s. (g) Transformation of the signal resulting from the measurement sequence (f) yields a sharp peak at the relative frequency $\Delta\nu$. (d)–(g) are reproduced from [141]. CC BY 4.0. (h) Persistence of saturated cwODMR contrast for C_x with magnetic field applied along the defect y direction. The solid curves represent the transition frequencies of the three ODMR transitions as a function of B_y amplitude. The measured cwODMR contrast as a function of MW frequency is represented by circles. (i) Angular magnetic-field dependence of cwODMR frequency (top panels) and normalised contrast of the three ODMR resonances of the C_x defect (top to bottom), with 50 mT bias magnetic field applied in the xy plane. Data are presented as circles and curves indicate the simulated cwODMR contrast. The inset indicates the direction of rotation of the bias magnetic field. (j) Calculated contrast of each resonance as a function of B_y and B_z. (k) Evolution of spin eigenstates with applied magnetic field along the x, y, z axes of the defect, from top to bottom. Calculated amplitudes of the optically initialised population of each spin sublevel are indicated by the size of the purple circles. (h)–(k) are reproduced from [118]. CC BY 4.0. All of the data was measured at 295 K.

improve the spin coherence and provide a tuneable sensor bandwidth for identification of a signal frequency. Pulsed [141, 172] and continuous [72] dynamic decoupling sequences have been shown to be effective for V_B^- ensembles and applied to sensing of MHz [141] and GHz [173] range magnetic signals, where the sensitivity ($\sim 1\ \mu\text{T}\sqrt{\text{Hz}}^{-1}$) can be comparable to that achieved with NV^- centres, when scaled by the volume of the sensor [173] (figures 3(c)–(g)). These sensing schemes have been extended to include advanced quantum heterodyne protocols that enable sensor frequency resolution far beyond the limit imposed by the spin coherence [141, 174].

While the V_B^- does not exhibit higher magnetic field susceptibility than the NV^- centre, recent results suggest it performs competitively, if not better, for sensing of temperature, pressure and electric field [160, 162, 175]. For temperature sensing, the longitudinal ZFS term (D) undergoes a 25-fold greater variation between room and cryogenic temperature than it does for the NV^- [160, 161]. This large effect is assigned to both temperature-dependent lattice distortion and second-order spin-phonon coupling [161]. D for the V_B^- is sensitive to in-plane pressure, but remarkably insensitive to out-of-plane pressure [160]. This has led to use of the V_B^- in diamond anvil cells for investigation of pressure-driven magnetism in other 2D materials [162, 176]. In contrast, it is the transverse ZFS parameter (E) for the V_B^- which is associated with sensitivity to electric field [175]. The electric field susceptibility is $d_\perp \sim 40\ \text{Hz}\,(\text{V cm})^{-1}$, roughly double that of the NV^- centre [177].

An emerging property of the V_B^- system for sensing, is that the defects retain their magneto-optical and sensing properties even in the few-layer ($\sim$3–5) limit [178]. This is unlike diamond where T_2^{echo} for NV^- centres starts to decrease when a defect is within 100 nm of the diamond surface [179]. This provides opportunities to develop atomically-thin sensing foils with hBN sensors.

3.3.2. Nanoscale quantum sensing

Nanoscale quantum sensing has been dominated by the NV^- centre with few other defect systems displaying adequate sensitivity on the single defect level, or the versatile operating conditions, to be serious candidates. The single carbon-related defects in hBN with $S = 1$ ODMR signatures provide a

feasible alternative to the NV^- centre. In particular, the C_x spin defect shows high brightness and ODMR on the single-defect level, which translates to $\mu T \sqrt{Hz}^{-1}$ DC sensitivity [36, 118], on par with the routinely achieved sensitivity for NV^- centres [150]. Unusually, the ODMR contrast for C_x is not completely quenched with high (>150 mT) off-axis magnetic field, which significantly increases the dynamic range for DC magnetometry over the NV^- centre [180]. Figure 3(h) shows the ODMR recorded for the C_x defect with an off-axis bias field up to 150 mT. As a result, C_x may open possibilities for the imaging of magnetic materials that require large, arbitrarily oriented bias fields to access emerging magnetic phenomena. The photophysical origin of the retention of ODMR contrast is related to the low symmetry of the defect (a property shared with other defects in diamond [181, 182]), which manifests as three measurable ODMR resonances (figures 3(i)–(k)) [118]. Each resonance displays a different dependence (in terms of quenching and sensitivity) to magnetic field orientation, providing the capability to perform vectorial magnetic field sensing [118].

Omnidirectional magnetic field sensing has been demonstrated with other single carbon-related defects that possess $S = 1/2$ spin signatures (the OSDP class) [62, 158]. Without a quantisation axis, these systems offer opportunities for facile detection of magnetic field strength, which might have useful applications in RF receivers for example [183], but no information on orientation, meaning extrapolation to magnetisation information is not possible, for example.

4. Defect structure identification

An immediate major challenge towards the development of defects in hBN for all technologies discussed so far is the elucidation of their atomic structure. Apart from the V_B^- and the C_BC_N UV emitter, the atomic structure of most defects is still under investigation. The assignment is complicated due to the disparity in optical properties and/or the lack of clear hyperfine signatures in ODMR spectra. However, conclusive confirmation of defect structure is critical for optimising operating conditions, refining the determinisitic fabrication process of these defects (which is discussed in detail in other reviews [4, 184, 185]), and advancing the fundamental understanding of their electronic properties. This demands joint efforts from theory and experiment.

4.1. *Ab initio* studies

First-principles calculations offer valuable microscopic insights into the electronic structure and the resulting spin and optical properties of solid state defects, including hBN [185, 186]. The workhorse of *ab initio* point defect studies in semiconductors is DFT, which has already proven its predictive power for formation energies [184], spin properties [185], and vibrational properties [187] in wide band gap semiconductors, including hBN [60, 70]. However, one needs to be cautious with the selection of DFT functionals [188] and when dealing with the excited state properties of defects. DFT is a mean-field ground state theory designed to accurately predict the ground state's total energy, density, spin density, and forces. Whereas, the measurable properties of spinless single-photon emitters in hBN, i.e. the UV [65], blue [76] and green–red [78] emitters, are linked to the excited state(s) of the defects.

Excited state properties can be approximated in DFT by forcing the occupation of the defect state to mimic an optical excitation of the centre. This procedure works reasonably well when the excited state can be described in the single-electron picture, i.e. exciting an electron from an occupied defect orbital to an empty defect orbital. The single electron picture may not be applicable for all defects, as the true many-particle wavefunction of the excited state can be formed as a linear combination of multiple single-particle transitions. Disregarding such state mixing in the optically excited states leads to an enhanced error in predicting ZPL energies, lifetimes, and decay rates, which can alter the identification of defects' microscopic structures.

Hexagonal boron nitride presents particular challenges in this respect. hBN features two types of states: the in-plane sp^2 hybrid bonding states (σ) and the out-of-plane p_z states (π) of the BN layers. A point defect can perturb both of these symmetrically distinguishable electronic states, often giving rise to a multitude of defect orbitals in the bandgap of hBN. For instance, the V_B^- center in hBN has twice as many active defect orbitals as the NV^- center in diamond, making the theoretical characterisation of the V_B^- center's excited state challenging [60, 124, 189]. Figure 4(a) presents the spin density of V_B^- as obtained by spin-polarised HSE06 DFT and figure 4(b) presents its single particle electronic structure. Generally, the number of single-particle defect states in the band gap indicates the complexity of the electronic structure and complex electronic structures may necessitate more advanced theoretical methods. The development and testing of post-DFT methods for hBN are currently at the forefront of theoretical studies [124, 189, 190]. Consolidating the necessary theoretical framework and solidifying theoretical predictions are expected to significantly contribute to successfully identifying the microscopic structure of the color centers in the not-so-distant future.

The rapid pace of experimental development, however, demands fast answers from theory. A viable approach is to focus on quantities that can be

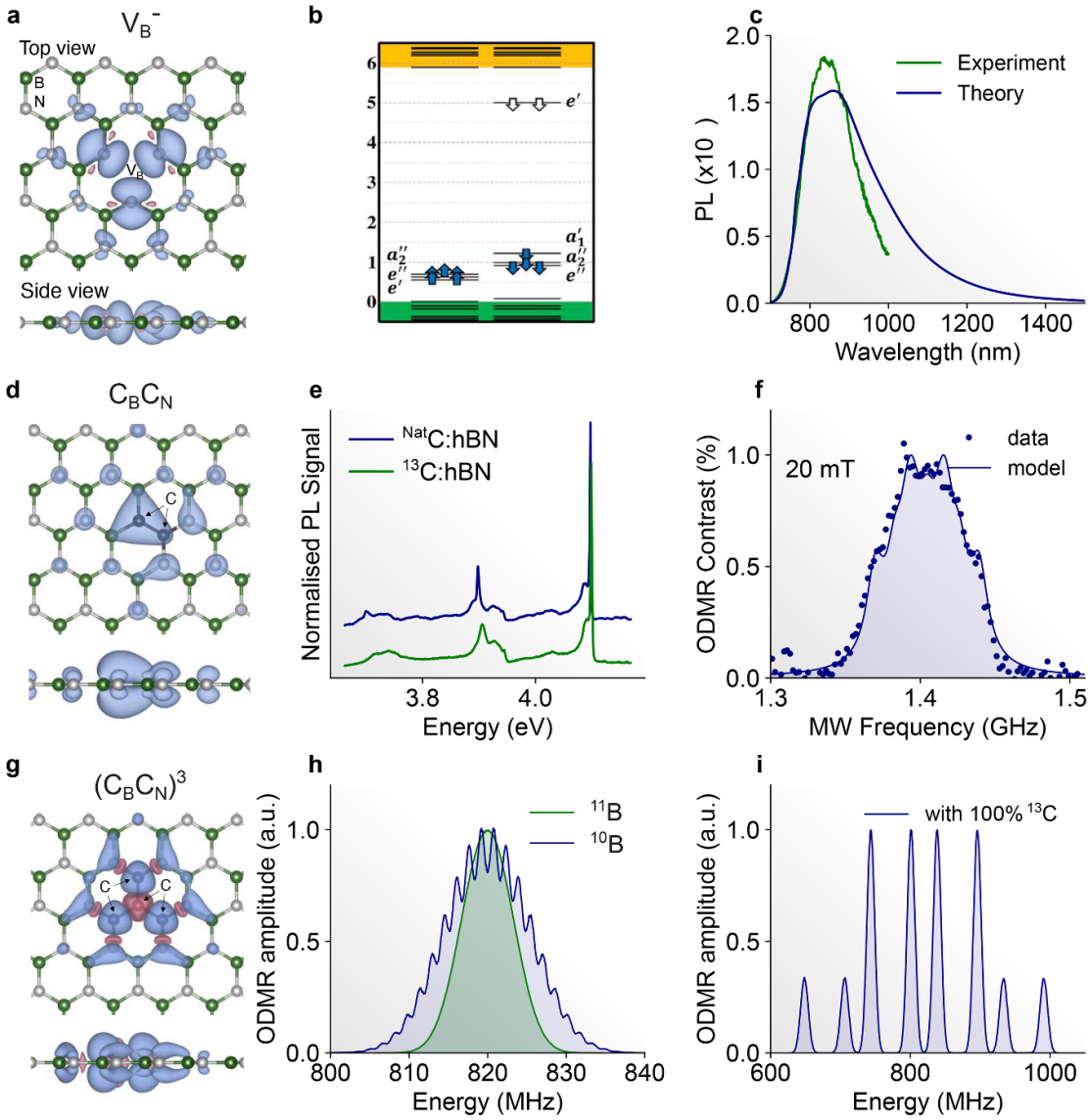

Figure 4. *Ab initio* modeling of hBN defects. (a) Spin density of V_B^- in hBN as obtained by spin-polarised HSE06 DFT. (b) Single particle electronic structure of the V_B^-, reproduced from [60]. CC BY 4.0. (c) Theoretical photoluminescence spectrum of the V_B^- compared to the experimental spectrum, reproduced from [60]. CC BY 4.0 and [33]. To produce the theoretical curve the calculated Huang-Rhys factor of 3.5 is used whereas the position of ZPL at 765 nm (1.62 eV) was aligned to match to the highest intensities of the experimental spectrum which corresponds to about 0.09 eV redshift compared to the KS DFT result (1.71 eV). (d) Spin density of C_BC_N. (e) Photoluminescence spectra measured at 8 K of the 'UV emitter' in two different isotopically enriched hBN samples, C_{nat}:hBN and ^{13}C:hBN. Reproduced from [70]. CC BY 4.0. (f) ODMR spectrum of the C_x defect, measured with 20-mT magnetic field parallel to the defect z axis. The dots are the data and the shaded curve is the computed spectrum. reproduced from [36]. CC BY 4.0. (g) Spin density of $(C_BC_N)^3$. (h) ODMR signal of the $(C_BC_N)^3$ defect at B = 0 mT with no carbon nuclear spins in ^{10}B (blue) and ^{11}B (green) containing samples. (i) ODMR signal of the $(C_BC_N)^3$ defect when it includes four ^{13}C nuclear spins. (i), (h) are reproduced from [191]. CC BY 4.0.

both reliably predicted by DFT methods and are experimentally accessible. For example, figure 4(c) compares the experimentally obtained and theoretically predicted PL spectra for the V_B^-. While ZPL energies can be inaccurate in DFT, polarisation angles and the fine structure of the phonon sideband can be obtained with reasonable accuracy [57, 187, 192]. Characteristic features of the polarisation of emitted/absorbed light are determined by the symmetry and orientation of the defect, providing relevant information about the underlying structure. The angle of the transition dipole and the lattice vectors for low-symmetry defect structures are parameters that can be compared with theoretical predictions [92]. The main features of the phonon sideband can be correlated with atomic masses, bond strength, and symmetry, serving as an optical fingerprint of the defect. When compared with high-resolution, low-temperature, and low-strain PL spectra, this can aid in the identification of the defect's microscopic structure. Furthermore, since the features of the phonon sideband depend on atomic masses,

isotope-engineered samples can provide further evidence of the atomic composition of the underlying structure [187]. These arguments motivate conducting in-depth experimental analyses of polarisation data and phonon sidebands, and placing greater emphasis on related DFT calculations in hBN. A very recent example of such a joint experimental theoretical work has been published in [70], where the microscopic structure of the UV emitter was studied and assigned to the C_BC_N complex (figures 4(d) and (e)). Here, this assignment was possible due to shifts in the phonon side bands in hBN isotopically enriched with ^{13}C, which were well modeled by simulation.

For spin-active defects, the hyperfine interaction with nearby nuclear spins and potentially the ZFS interaction provide another, very reliable means of identification. Indeed, the direction of the preferential quantisation axis of the electron spin and value of D and E carry important information on the symmetry of the defect and the degree of spin density localisation. The hyperfine splitting of the spin sublevels due to strongly coupled nuclear spin(s) serves as a unique fingerprint of the defect that can be accurately calculated in reliable ground state DFT calculations [193, 194]. This enabled identification of the V_B^- center [33, 60].

Assignment of the single carbon-related spin defects has been more difficult. The C_x defects show a narrow ESR/ODMR linewidth at zero field [36] compared to the V_B^-. This is consistent both with the low symmetry of C_x combined with localisation of the electron spin density on spin-less ^{12}C carbon atoms which appears in ∼0.99 probability in natural abundance. However, the hyperfine structure at higher field has been difficult to assign to a particular structure. Figure 4(f) shows the ODMR spectrum of the C_x centre with an aligned magnetic field of 20 mT. The fit is a modeled spectrum, which considers the defect is coupled to two nonequivalent nuclei. For carbon-based defects, the use of $S = 1/2$ ^{13}C enriched carbon sources during growth or implantation could give rise to a resolvable hyperfine structure. Such a hyperfine spectrum alone could declare the number of carbon atoms in the structure, while DFT calculations could nail down the microscopic configuration. This has been demonstrated by theoretical studies of carbon tetramers (not yet assigned to experimentally observed spin defects) [191] (figures 4(h)–(i)). This approach has also been successful experimentally; Gao *et al* has observed hyperfine splittings in ^{13}C implanted and annealed hBN, which helped to narrow down the possible defect configurations to DAP complexes [63].

Based on the challenges and methodologies discussed above, we propose the following joint theoretical-experimental workflow for identifying point defects in hBN:

- Basic electronic structure assessment: perform ground-state DFT calculations to determine formation energies and geometries for candidates motivated by growth and fabrication conditions, or alternatively, employ high-throughput DFT screening. Analyze formation energies and single-particle defect orbitals in the band gap to rule out unlikely candidates. Use DFT to calculate ground-state spin properties, but employ post-DFT methods (e.g. CI, GW-BSE) for the final assessment of optical properties.
- Color center identification: correlate experimental emission polarisation angles with theoretical transition dipole orientations to determine defect symmetry and lattice orientation. Compare high-resolution, low-temperature PL phonon sidebands with calculated vibrational modes. Focus on the phonon sidebands' fine structure rather than the absolute ZPL energy, as the former serves as a robust fingerprint of bond strengths and atomic masses.
- Paramagnetic defect identification: for spin-active defects, measure the ZFS parameters and hyperfine interactions via ODMR/ESR. Compare these results with ground-state DFT predictions. The quantization axis reveals the defect symmetry, while the hyperfine interaction values, which can be accurately obtained via DFT, provide a map of the local nuclear environment.
- Verification by isotopic enrichment: fabricate isotopically enriched samples (e.g. ^{10}B, ^{13}C, ^{15}N). Identify specific shifts in the phonon sideband or the emergence/splitting of hyperfine lines in spin resonance spectra. Match these shifts with theoretical simulations of the isotope-modified structure to definitively confirm the atomic composition of the defect.

4.2. Electron and x-ray beam imaging

Beyond DFT, electron and x-ray microscopies have been used—in some cases correlated with PL—to gain insight to atomic structure [195–197]. In general, the challenge here is correlation of optical and x-ray/electron microscopy images, which have different spatial resolution limits. A combined study of cathodoluminescence, PL and electron microscopy presented a complex picture of multiple defect types contributing to the green–red emitter family, but could not propose specific chemical structures [195]. Resonant inelastic x-ray scattering has been recently used to identify a common elementary excitation at 285 meV for hBN green–red single-photon emitters [197]. These results point towards the importance of the N π^* anti-bonding orbitals in defining the optical properties of hBN defects that emit in the visible region. High resolution scanning transmission

electron microscopy in conjunction with confocal imaging and elemental mapping (EELS) has imaged carbon complexes formed in 60 nm thick exfoliated hBN flakes [196]. It was observed that carbon readily replaces nitrogen and boron in the hBN lattice, and several potential carbon-related structures (carbon dimers and single carbon substitutions) were proposed. To date, all correlative studies of this nature have struggled with unambiguous identification of atomic structure of the emissive/spin active defects due to the density of non-emissive defects. Future attempts will need to utilise other ways to get around this problem, possibly with ultra high purity hBN, or using nanoscale probes/markers to aid the correlation.

4.3. Defect creation

A common, longstanding challenge for the realisation of quantum technologies based on defects is the controllable, spatially-deterministic defect fabrication. This is important for coupling defects accurately to photonic/electrical components, or nanostructures, in a device. A major appeal of 2D material platforms is their potential for achieving new routes to achieving high control over the fabrication of defects. Below we summarise the work so far in this direction for both defect ensembles (V_B^-) and carbon-related defects.

4.3.1. Boron vacancies

V_B^- ensembles are typically fabricated through controlled defect engineering techniques that selectively remove boron atoms, most commonly electron [198, 199], ion [200, 201], neutron [33] and laser irradiation [202, 203]. In the case of neutron irradiation, efficient vacancy generation relies on the large neutron capture cross section of the ^{10}B isotope; consequently, this method is only effective for hBN with a significant ^{10}B isotopic content. This includes hBN of natural abundance (20% ^{10}B), but not isotopically purified h^{11}BN.

A major advantage of neutron irradiation is its ability to produce a uniform defect density throughout bulk hBN flakes, which can subsequently be exfoliated and integrated into devices without significantly altering the vacancy distribution. By contrast, ion implantation is compatible with semiconductor workflows, but the depth distribution of the defects exhibits a strong dependence on flake thickness, underlying substrate, and the implantation parameters (e.g. ion species, energy, temperature and dose) [204–206]. As a result, achieving reproducible films typically requires a more complex workflow: flakes of a targeted thickness must first be prepared on a well-defined substrate, then irradiated under optimised conditions, and then transferred into the system of interest.

Work is ongoing to optimise the V_B^- density for sensing (see section 3.3), where there is a trade-off between increasing the photoluminesence signal and introducing damage to the hBN lattice that degrades the coherence properties [207–209]. To fully exploit the key advantage of hBN for sensing, the ability of extremely thin samples to host spin defects [178], this optimisation should focus on V_B^- ensembles in ultrathin hBN. In this regime, additional factors such as the sensor-sample stand-off distance, photon extraction efficiency [210], charge state control [211, 212] and near-field effects [213] must also be taken into account.

4.3.2. Carbon-related defects

Site-specific and deterministic creation of visible emitting, suspected carbon-related, defects has been a longstanding goal. Early efforts explored the use of strain [214] to create localised deformation potentials to 'activate' defects in a near-deterministic fashion. Site-specific fabrication of single 'B-centres' has been demonstrated via focused electron beam irradiation [68]. This technique enables x–y spatial resolution on the sub-micron level but limited control of the depth of defect creation. Unlike most other defect creation efforts, this work developed a process that preferentially creates 'B-centres' over other defect species.

The controlled engineering of spin-active carbon related defects is less well developed, but vital for their target applications. To date, most spin-active carbon-relate defects have been formed via *in-situ* carbon doping of multilayer hBN. For example, reports of OSDPs have come mainly from multilayer films that are grown via MOVPE, chemical vapour deposition (CVD) or molecular beam epitaxy [114]. In these techniques, carbon is introduced during the growth process either as a carbon-based precursor or via evaporation of carbon in the chamber [78]. These techniques allow for control over the degree of carbon doping, but no control over the spatial incorporation of carbon in the film. This clearly presents a challenge for their incorporation to scalable quantum devices.

Single C_x defects are found at low density ($\sim$1 per μm^2) in MOVPE-grown films [36, 38, 78], but as yet there have been no detailed studies to control defect density or placement. CC/CO DAP-X defects have been fabricated with an ion-implantation and annealing process [63]. Combined with lithographic patterning this could provide a route to deterministic positional control.

Development of defect creation techniques that enable specificity for given spin defects with submicron spatial control will unlock routes to incorporate them in devices. For sensing this will enable fabrication of probes for nanoscale magnetometry, and for optical techniques this is will make it easier to couple the defects to waveguides and cavities to boost optical emission. Techniques such as laser writing [41], ion-implantation and focused electron beam irradiation should be explored further. However, knowledge of the defects' atomic structure will be critical in this

regard, and currently provides a significant challenge to the development of fabrication methods.

5. Conclusion

We consider that hBN defects present an exciting novel platform to explore for future quantum technologies. While significant further technical development is required before hBN defects will be deployed for quantum computing or repeaters for optical networks, in our view there are several applications where hBN defects can outperform alternative candidates in the near term.

The first is quantum sensing, specifically *in-situ* quantum sensing in 2D heterostructures and nanoscale sensing. With regards to the former, hBN already forms a critical dielectric component of most 2D heterostructure devices. If high concentrations of defects (either V_B^- or single defects) can be engineered atomically close to the surface of hBN layers, that are then incorporated within devices, *in-situ* hBN quantum sensors could be useful for exploration of magnetic phenomena, stress gradients, or charge flow in these devices as well as routine methods of device quality control, for example.

For nanoscale sensing, single carbon-related hBN defects offer the potential for nm-spatial resolution. This is an attractive proposition, as for NV^- scanning magnetometry, typical spatial resolution is 20–30 nm [150], due to the difficulty in fabricating single NVs close to the apex of a diamond tip and the degradation of magneto-optical properties for shallow NV^- centres. In addition, single C_x hBN defects operate under off-axis bias magnetic field of 100's mT. This may enable investigation of new material systems, or reveal new insight to nanoscale spin textures in other materials. Although the full picture is still emerging, the range of different carbon-related single spin defects points towards future opportunities to engineer specific sensors where the spin multiplicity, ZFS magnitude and orientation of the spin quantisation axis could be designed for the sensing application. For example, the presence of defects with quantisation axes aligned to or perpendicular to the 2D layers makes the alignment of bias fields more straightforward.

A second key area is likely to be free-space and satellite-based QKD. The high repetition rates, linear polarisation and broad range of emission wavelengths make hBN defects key contenders in this area. However, electrical excitation as well as ZPL tuneability will need to become established as routine capabilities.

Finally, future progress across all areas will be contingent on understanding how to control the creation of hBN defects in different hBN materials. There are already promising signs that defect creation can be controlled via external treatment (ion/electron beam/annealing) of hBN exfoliated crystals, or carbon-doping of CVD material. Early efforts to create defects in hBN with spatial control are promising [68, 69, 215], but precise site-control is still needed. Defect creation attempts would benefit from identification of unknown defect structures, namely the green–red emitting family that shows ODMR. It is our view that coordinating experimental spin resonance, with *Ab initio* studies and materials characterisation, should lead to many of these defects being assigned structures in the near future.

Acknowledgments

We acknowledge Andrew Ramsey for helpful discussions.

T V acknowledges acknowledges support from the Munich Quantum Valley, which is supported by the Bavarian state government with funds from the Hightech Agenda Bayern Plus.

V I acknowledges support from the National Research, Development and Innovation Office of Hungary (NKFIH) within the Quantum Information National Laboratory of Hungary (Grant No. 2022-2.1.1-NL-2022-00004) and the Project FK 145395. This project is funded by the European Commission within Horizon Europe projects (Grant Nos. 101156088 and 101129663).

H L S acknowledges support from a Royal Society University Research Fellowship (URF RI 221326) and the UKRI EPSRC projects (Grant Nos. APP17698 and APP51824).

Data availability statement

The data cannot be made publicly available upon publication because they are owned by a third party and the terms of use prevent public distribution. The data that support the findings of this study are available upon reasonable request from the authors.

ORCID iDs

Tobias Vogl 0000-0002-0993-0648
Viktor Ivády 0000-0003-0111-5101
Isaac J Luxmoore 0000-0002-2650-0842
Hannah L Stern 0000-0001-6516-4805

References

[1] Becher C *et al* 2023 2023 roadmap for materials for quantum technologies *Mater. Quantum Technol.* **3** 012501
[2] Awschalom D D, Hanson R, Wrachtrup J and Zhou B B 2018 Quantum technologies with optically interfaced solid-state spins *Nat. Photon.* **12** 516–27
[3] Atatüre M, Englund D, Vamivakas N, Lee S Y and Wrachtrup J 2018 Material platforms for spin-based photonic quantum technologies *Nat. Rev. Mater.* **3** 38–51

[4] Wolfowicz G, Heremans F J, Anderson C P, Kanai S, Seo H, Gali A, Galli G and Awschalom D D 2021 Quantum guidelines for solid-state spin defects *Nat. Rev. Mater.* **6** 906–25

[5] O'Brien J L 2007 Optical quantum computing *Science* **318** 1567–70

[6] Hanson R and Awschalom D D 2008 Coherent manipulation of single spins in semiconductors *Nature* **453** 1043–9

[7] Couteau C, Barz S, Durt T, Gerrits T, Huwer J, Prevedel R, Rarity J, Shields A and Weihs G 2023 Applications of single photons to quantum communication and computing *Nat. Rev. Phys.* **5** 326–38

[8] DiVincenzo D P 2000 The physical implementation of quantum computation *Fortschr. Phys.* **48** 771–83

[9] Schirhagl R, Chang K, Loretz M and Degen C L 2014 Nitrogen-vacancy centers in diamond: nanoscale sensors for physics and biology *Annu. Rev. Phys. Chem.* **65** 83–105

[10] Vaidya S, Gao X, Dikshit S, Aharonovich I and Li T 2023 Quantum sensing and imaging with spin defects in hexagonal boron nitride *Adv. Phys. X* **8** 2206049

[11] Kimble H J 2008 The quantum internet *Nature* **453** 1023–30

[12] Doherty M W, Manson N B, Delaney P, Jelezko F, Wrachtrup J and Hollenberg L C L 2013 The nitrogen-vacancy colour centre in diamond *Phys. Rep.* **528** 1–45

[13] Togan E *et al* 2010 Quantum entanglement between an optical photon and a solid-state spin qubit *Nature* **466** 730–4

[14] Bernien H *et al* 2013 Heralded entanglement between solid-state qubits separated by three metres *Nature* **497** 86–90

[15] Humphreys P C, Kalb N, Morits J P J, Schouten R N, Vermeulen R F L, Twitchen D J, Markham M and Hanson R 2018 Deterministic delivery of remote entanglement on a quantum network *Nature* **558** 268–73

[16] Pompili M *et al* 2021 Realization of a multinode quantum network of remote solid-state qubits *Science* **372** 259–64

[17] Dutt M V G, Childress L, Jiang L, Togan E, Maze J, Jelezko F, Zibrov A S, Hemmer P R and Lukin M D 2007 Quantum register based on individual electronic and nuclear spin qubits in diamond *Science* **316** 1312–6

[18] Taminiau T H, Cramer J, Sar T V D, Dobrovitski V V and Hanson R 2014 universal control and error correction in multi-qubit spin registers in diamond *Nat. Nanotechnol.* **9** 171–6

[19] Bradley C E, Randall J, Abobeih M H, Berrevoets R C, Degen M J, Bakker M A, Markham M, Twitchen D J and Taminiau T H 2019 A ten-qubit solid-state spin register with quantum memory up to one minute *Phys. Rev. X* **9** 031045

[20] Chernobrod B M and Berman G P 2005 Spin microscope based on optically detected magnetic resonance *J. Appl. Phys.* **97** 014903

[21] Taylor J M, Cappellaro P, Childress L, Jiang L, Budker D, Hemmer P R, Yacoby A, Walsworth R and Lukin M D 2008 High-sensitivity diamond magnetometer with nanoscale resolution *Nat. Phys.* **4** 810–6

[22] Degen C L 2008 Scanning magnetic field microscope with a diamond single-spin sensor *Appl. Phys. Lett.* **92** 243111

[23] Degen C L, Reinhard F and Cappellaro P 2017 Quantum sensing *Rev. Mod. Phys.* **89** 035002

[24] Koehl W F, Buckley B B, Heremans F J, Calusine G and Awschalom D D 2011 Room temperature coherent control of defect spin qubits in silicon carbide *Nature* **479** 84–87

[25] Bourassa A *et al* 2020 Entanglement and control of single nuclear spins in isotopically engineered silicon carbide *Nat. Mater.* **19** 1319–25

[26] Redjem W *et al* 2020 Single artificial atoms in silicon emitting at telecom wavelengths *Nat. Electron.* **3** 738–43

[27] Higginbottom D B *et al* 2022 Optical observation of single spins in silicon *Nature* **607** 266–70

[28] Simmons S 2024 Scalable fault-tolerant quantum technologies with silicon color centers *PRX Quantum* **5** 010102

[29] Durand A *et al* 2024 Genuine and faux single g centers in carbon-implanted silicon *Phys. Rev. B* **110** L020102

[30] Luo J, Geng Y, Rana F and Fuchs G D 2024 Room temperature optically detected magnetic resonance of single spins in gan *Nat. Mater.* **23** 512–8

[31] Tran T T, Bray K, Ford M J, Toth M and Aharonovich I 2016 Quantum emission from hexagonal boron nitride monolayers *Nat. Nanotechnol.* **11** 37–41

[32] Aharonovich I, Englund D and Toth M 2016 Solid-state single-photon emitters *Nat. Photon.* **10** 631–41

[33] Gottscholl A *et al* 2020 Initialisation and read-out of intrinsic spin defects in a van der Waals crystal at room temperature *Nat. Mater.* **19** 540–5

[34] Chejanovsky N *et al* 2021 Single-spin resonance in a van der Waals embedded paramagnetic defect *Nat. Mater.* **20** 1079–84

[35] Stern H L *et al* 2022 Room-temperature optically detected magnetic resonance of single defects in hexagonal boron nitride *Nat. Commun.* **13** 618

[36] Stern H L *et al* 2024 A quantum coherent spin in hexagonal boron nitride at ambient conditions *Nat. Mater.* **23** 1379–85

[37] Kim S M *et al* 2015 Synthesis of large-area multilayer hexagonal boron nitride for high material performance *Nat. Commun.* **6** 8662

[38] Chugh D, Wong-Leung J, Li L, Lysevych M, Tan H H and Jagadish C 2018 Flow modulation epitaxy of hexagonal boron nitride *2D Mater.* **5** 045018

[39] Lee J S *et al* 2018 Wafer-scale single-crystal hexagonal boron nitride film via self-collimated grain formation *Science* **362** 817–21

[40] Wang L *et al* 2019 Epitaxial growth of a 100-square-centimetre single-crystal hexagonal boron nitride monolayer on copper *Nature* **570** 91–95

[41] Wang Y *et al* 2024 Ultraflat single-crystal hexagonal boron nitride for wafer-scale integration of a 2D-compatible high-κ metal gate *Nat. Mater.* **23** 1495

[42] Novoselov K S, Mishchenko A, Carvalho A and Neto A H C 2016 2D materials and van der Waals heterostructures *Science* **353** 9439

[43] Fukamachi S, Solís-Fernández P, Kawahara K, Tanaka D, Otake T, Lin Y-C, Suenaga K and Ago H 2023 Large-area synthesis and transfer of multilayer hexagonal boron nitride for enhanced graphene device arrays *Nat. Electron.* **6** 126–36

[44] Li C, Fröch J E, Nonahal M, Tran T N, Toth M, Kim S and Aharonovich I 2021 Integration of hBN quantum emitters in monolithically fabricated waveguides *ACS Photonics* **8** 2966–72

[45] Kim S, Fröch J E, Christian J, Straw M, Bishop J, Totonjian D, Watanabe K, Taniguchi T, Toth M and Aharonovich I 2018 Photonic crystal cavities from hexagonal boron nitride *Nat. Commun.* **9** 2623

[46] Vogl T, Lecamwasam R, Buchler B C, Lu Y and Lam P K 2019 Compact cavity-enhanced single-photon generation with hexagonal boron nitride *ACS Photonics* **6** 1955–62

[47] Fröch J E, Spencer L P, Kianinia M, Totonjian D D, Nguyen M, Gottscholl A, Dyakonov V, Toth M, Kim S and Aharonovich I 2021 Coupling spin defects in hexagonal boron nitride to monolithic bullseye cavities *Nano Lett.* **21** 6549–55

[48] Blascetta N P, Liebel M, Lu X, Taniguchi T, Watanabe K, Efetov D K and Hulst N F V 2020 Nanoscale imaging and control of hexagonal boron nitride single photon emitters by a resonant nanoantenna *Nano Lett.* **20** 1992–9

[49] Noh G, Choi D, Kim J-H, Im D-G, Kim Y-H, Seo H and Lee J 2018 Stark tuning of single-photon emitters in hexagonal boron nitride *Nano Lett.* **18** 4710–5

[50] Akbari H, Biswas S, Jha P K, Wong J, Vest B and Atwater H A 2022 Lifetime-limited and tunable quantum light emission in h-BN via electric field modulation *Nano Lett.* **22** 7798–803

[51] Zhigulin I, Park G, Yamamura K, Watanabe K, Taniguchi T, Toth M, Kim J and Aharonovich I 2025 Electrical generation of color centers in hexagonal boron nitride *ACS Appl. Mater. Interfaces* **17** 24129–36
[52] Jungwirth N R and Fuchs G D 2017 Optical absorption and emission mechanisms of single defects in hexagonal boron nitride *Phys. Rev. Lett.* **119** 057401
[53] Arı O, Polat N, Fırat V, Çakır O and Ateş S 2025 Temperature-dependent spectral properties of hexagonal boron nitride color centers *ACS Photonics* **12** 1676–82
[54] Grosso G, Moon H, Lienhard B, Ali S, Efetov D K, Furchi M M, Jarillo-Herrero P, Ford M J, Aharonovich I and Englund D 2017 Tunable and high-purity room temperature single-photon emission from atomic defects in hexagonal boron nitride *Nat. Commun.* **8** 705
[55] Liu W, Wang Y T, Li Z P, Yu S, Ke Z J, Meng Y, Tang J S, Li C F and Guo G C 2020 An ultrastable and robust single-photon emitter in hexagonal boron nitride *Physica E* **124** 114251
[56] Guo N J *et al* 2023 Coherent control of an ultrabright single spin in hexagonal boron nitride at room temperature *Nat. Commun.* **14** 2893
[57] Kumar A *et al* 2024 Polarization dynamics of solid-state quantum emitters *ACS Nano* **18** 5270–81
[58] Gottscholl A, Diez M, Soltamov V, Kasper C, Sperlich A, Kianinia M, Bradac C, Aharonovich I and Dyakonov V 2021 Room temperature coherent control of spin defects in hexagonal boron nitride *Sci. Adv.* **7** 3630
[59] Exarhos A L, Hopper D A, Patel R N, Doherty M W and Bassett L C 2019 Magnetic-field-dependent quantum emission in hexagonal boron nitride at room temperature *Nat. Commun.* **10** 222
[60] Ivády V, Barcza G, Thiering G, Li S, Hamdi H, Chou J P, Legeza O and Gali A 2020 Ab initio theory of the negatively charged boron vacancy qubit in hexagonal boron nitride *npj Comput. Mater.* **6** 41
[61] Gong R *et al* 2024 Isotope engineering for spin defects in van der Waals materials *Nat. Commun.* **15** 104
[62] Scholten S C *et al* 2024 Multi-species optically addressable spin defects in a van der Waals material *Nat. Commun.* **15** 6727
[63] Gao X, Sumukh S, Li K, Ge Z, Dikshit S, Zhang S, Shen P J, Jin Y, Ping Y and Li T 2025 Single nuclear spin detection and control in a van der Waals material *Nature* **643** 943–9
[64] Gisin N, Ribordy G, Tittel W and Zbinden H 2002 Quantum cryptography *Rev. Mod. Phys.* **74** 145–95
[65] Bourrellier R, Meuret S, Tararan A, Stéphan O, Kociak M, Tizei L H G and Zobelli A 2016 Bright uv single photon emission at point defects in h-BN *Nano Lett.* **16** 4317–21
[66] Tran T T, Elbadawi C, Totonjian D, Lobo C J, Grosso G, Moon H, Englund D R, Ford M J, Aharonovich I and Toth M 2016 Robust multicolor single photon emission from point defects in hexagonal boron nitride *ACS Nano* **10** 7331–8
[67] Camphausen R, Marini L, Tawfik S A, Tran T T, Ford M J and Palomba S 2020 Observation of near-infrared sub-Poissonian photon emission in hexagonal boron nitride at room temperature *APL Photonics* **5** 076103
[68] Gale A, Li C, Chen Y, Watanabe K, Taniguchi T, Aharonovich I and Toth M 2022 Site-specific fabrication of blue quantum emitters in hexagonal boron nitride *ACS Photonics* **9** 2170–7
[69] Kumar A, Cholsuk C, Zand A, Mishuk M N, Matthes T, Eilenberger F, Suwanna S and Vogl T 2023 Localized creation of yellow single photon emitting carbon complexes in hexagonal boron nitride *APL Mater.* **11** 071108
[70] Plo J *et al* 2025 Isotope substitution and polytype control for point defects identification: the case of the ultraviolet color center in hexagonal boron nitride *Phys. Rev. X* **15** 021045
[71] Fournier C *et al* 2021 Position-controlled quantum emitters with reproducible emission wavelength in hexagonal boron nitride *Nat. Commun.* **12** 3779
[72] Ramsay A J, Hekmati R, Patrickson C J, Baber S, Arvidsson-Shukur D R M, Bennett A J and Luxmoore I J 2023 Coherence protection of spin qubits in hexagonal boron nitride *Nat. Commun.* **14** 461
[73] Fournier C, Roux S, Watanabe K, Taniguchi T, Buil S, Barjon J, Hermier J-P and Delteil A 2023 Two-photon interference from a quantum emitter in hexagonal boron nitride *Phys. Rev. Appl.* **19** L041003
[74] Vuong T Q P, Cassabois G, Valvin P, Ouerghi A, Chassagneux Y, Voisin C and Gil B 2016 Phonon-photon mapping in a color center in hexagonal boron nitride *Phys. Rev. Lett.* **117** 071108
[75] Li S, Pershin A, Thiering G, Udvarhelyi P and Gali A 2022 Ultraviolet quantum emitters in hexagonal boron nitride from carbon clusters *J. Phys. Chem. Lett.* **13** 3150–7
[76] Zhigulin I, Yamamura K, Ivády V, Gale A, Horder J, Lobo C J, Kianinia M, Toth M and Aharonovich I 2023 Photophysics of blue quantum emitters in hexagonal boron nitride *Mater. Quantum Technol.* **3** 015002
[77] Yamamura K, Coste N, Zeng H Z J, Toth M, Kianinia M and Aharonovich I 2025 Quantum efficiency of the B-centre in hexagonal boron nitride *Nanophotonics* **14** 1715–20
[78] Mendelson N *et al* 2021 Identifying carbon as the source of visible single-photon emission from hexagonal boron nitride *Nat. Mater.* **20** 321–8
[79] Maciaszek M and Razinkovas L 2024 Blue quantum emitter in hexagonal boron nitride and a carbon chain tetramer: a first-principles study *ACS Appl. Nano Mater.* **7** 18979–85
[80] Nikolay N, Mendelson N, Özelci E, Sontheimer B, Böhm F, Kewes G, Toth M, Aharonovich I and Benson O 2019 Direct measurement of quantum efficiency of single-photon emitters in hexagonal boron nitride *Optica* **6** 1084–8
[81] Bommer A and Becher C 2019 New insights into nonclassical light emission from defects in multi-layer hexagonal boron nitride *Nanophotonics* **8** 2041–8
[82] Chatterjee A, Biswas A, Fuhr A S, Terlier T, Sumpter B G, Ajayan P M, Aharonovich I and Huang S 2025 Room-temperature high-purity single-photon emission from carbon-doped boron nitride thin films *Sci. Adv.* **11** 899
[83] Dong S, Mi S, Hou Q, Huang Y, Wang J, Yu Y, Wei Z, Zhang Z and Fang J 2023 Decoy state semi-quantum key distribution *EPJ Quantum Technol.* **10** 230504
[84] Li H-W, Zhang C-M, Jiang M-S and Cai Q-Y 2022 Improving the performance of practical decoy-state quantum key distribution with advantage distillation technology *Commun. Phys.* **5** 53
[85] Samaner Ç, Paçal S, Mutlu G, Uyanık K and Ateş S 2022 Free-space quantum key distribution with single photons from defects in hexagonal boron nitride *Adv. Quantum Technol.* **5** 2200059
[86] Al-Juboori A, Zeng H Z J, Nguyen M A P, Ai X, Laucht A, Solntsev A, Toth M, Malaney R and Aharonovich I 2023 Quantum key distribution using a quantum emitter in hexagonal boron nitride *Adv. Quantum Technol.* **6** 2300038
[87] Häußler S, Bayer G, Waltrich R, Mendelson N, Li C, Hunger D, Aharonovich I and Kubanek A 2021 Tunable fiber-cavity enhanced photon emission from defect centers in hBN *Adv. Opt. Mater.* **9** 2002218
[88] Vogl T, Knopf H, Weissflog M, Lam P K and Eilenberger F 2021 Sensitive single-photon test of extended quantum theory with two-dimensional hexagonal boron nitride *Phys. Rev. Res.* **3** 013296
[89] Abasifard M, Cholsuk C, Pousa R G, Kumar A, Zand A, Riel T, Oi D K L and Vogl T 2024 The ideal wavelength for daylight free-space quantum key distribution *APL Quantum* **1** 016113
[90] Liao S-K *et al* 2017 Satellite-to-ground quantum key distribution *Nature* **549** 43–47
[91] Cholsuk C, Suwanna S and Vogl T 2022 Tailoring the emission wavelength of color centers in hexagonal

boron nitride for quantum applications *Nanomaterials* **12** 2427
[92] Cholsuk C, Zand A, Çakan A and Vogl T 2024 The hBN defects database: a theoretical compilation of color centers in hexagonal boron nitride *J. Phys. Chem. C* **128** 12716–25
[93] Dhu-al Shaik A B, Palla P and Jenkins D 2024 Electrical tuning of quantum light emitters in hBN for free space and telecom optical bands *Sci. Rep.* **14** 811
[94] Wang J-F *et al* 2020 Coherent control of nitrogen-vacancy center spins in silicon carbide at room temperature *Phys. Rev. Lett.* **124** 223601
[95] Higginbottom D B, Asadi F K, Chartrand C, Ji J W, Bergeron L, Thewalt M L W, Simon C and Simmons S 2023 Memory and transduction prospects for silicon *T* center devices *PRX Quantum* **4** 020308
[96] Zhao H, Pettes M T, Zheng Y and Htoon H 2021 Site-controlled telecom-wavelength single-photon emitters in atomically-thin $MoTe_2$ *Nat. Commun.* **12** 6753
[97] Vogl T, Lu Y and Lam P K 2017 Room temperature single photon source using fiber-integrated hexagonal boron nitride *J. Phys. D: Appl. Phys.* **50** 295101
[98] Schmitt-Manderbach T *et al* 2007 Experimental demonstration of free-space decoy-state quantum key distribution over 144 km *Phys. Rev. Lett.* **98** 010504
[99] Vogl T, Campbell G, Buchler B C, Lu Y and Lam P K 2018 Fabrication and deterministic transfer of high-quality quantum emitters in hexagonal boron nitride *ACS Photonics* **5** 2305–12
[100] Vest G, Freiwang P, Luhn J, Vogl T, Rau M, Knips L, Rosenfeld W and Weinfurter H 2022 Quantum key distribution with a hand-held sender unit *Phys. Rev. Appl.* **18** 024067
[101] Vogl T *et al* 2019 Radiation tolerance of two-dimensional material-based devices for space applications *Nat. Commun.* **10** 1202
[102] Ahmadi N *et al* 2024 Quick^3—design of a satellite-based quantum light source for quantum communication and extended physical theory tests in space *Adv. Quantum Technol.* **7** 2300343
[103] Zhigulin I, Horder J, Ivády V, Iteite S J U, Gale A, Li C, Lobo C J, Toth M, Aharonovich I and Kianinia M 2023 Stark effect of blue quantum emitters in hexagonal boron nitride *Phys. Rev. Appl.* **19** 044011
[104] Grzeszczyk M, Vaklinova K, Watanabe K, Taniguchi T, Novoselov K S and Koperski M 2023 Electrical excitation of carbon centers in hexagonal boron nitride with tuneable quantum efficiency (arXiv:2305.13679)
[105] Yu M, Lee J, Watanabe K, Taniguchi T and Lee J 2025 Electrical pumping of h-BN single-photon sources in van der Waals heterostructures *ACS Nano* **19** 504–11
[106] Kok P, Munro W J, Nemoto K, Ralph T C, Dowling J P and Milburn G J 2007 Linear optical quantum computing with photonic qubits *Rev. Mod. Phys.* **79** 135–74
[107] Raussendorf R and Briegel H J 2001 A one-way quantum computer *Phys. Rev. Lett.* **86** 5188–91
[108] White S, Stewart C, Solntsev A S, Li C, Toth M, Kianinia M and Aharonovich I 2021 Phonon dephasing and spectral diffusion of quantum emitters in hexagonal boron nitride *Optica* **8** 1153–8
[109] Koch M K, Bharadwaj V and Kubanek A 2024 Probing the limits for coherent optical control of a mechanically decoupled defect center in hexagonal boron nitride *Commun. Mater.* **5** 240
[110] Hoese M, Reddy P, Dietrich A, Koch M K, Fehler K G, Doherty M W and Kubanek A 2020 Mechanical decoupling of quantum emitters in hexagonal boron nitride from low-energy phonon modes *Sci. Adv.* **6** 6038
[111] Dietrich A, Doherty M W, Aharonovich I and Kubanek A 2020 Solid-state single photon source with fourier transform limited lines at room temperature *Phys. Rev. B* **101** 081401
[112] Grange T, Hornecker G, Hunger D, Poizat J-P, Gérard J-M, Senellart P and Auffèves A 2015 Cavity-funneled generation of indistinguishable single photons from strongly dissipative quantum emitters *Phys. Rev. Lett.* **114** 193601
[113] Conlon L O *et al* 2023 Approaching optimal entangling collective measurements on quantum computing platforms *Nat. Phys.* **19** 351–7
[114] Scholten S C *et al* 2025 Optically detected magnetic resonance of wafer-scale hexagonal boron nitride thin films *Mater. Quantum. Technol.* **5** 045701
[115] Gao X *et al* 2022 Nuclear spin polarization and control in hexagonal boron nitride *Nat. Mater.* **21** 1024–8
[116] Robertson I O *et al* 2025 A charge transfer mechanism for optically addressable solid-state spin pairs *Nat. Phys.* **21** 1981–7
[117] Singh P *et al* 2025 Violet to near-infrared optical addressing of spin pairs in hexagonal boron nitride *Adv. Mater.* **37** 2414846
[118] Gilardoni C M *et al* 2025 A single spin in hexagonal boron nitride for vectorial quantum magnetometry *Nat. Commun.* **16** 4947
[119] Gao X, Ge Z, Dikshit S, Vaidya S, Ju P and Li T 2025 Room-temperature quantum entanglement in a van der Waals material (arXiv:2509.23170v1)
[120] Bar-Gill N, Pham L M, Jarmola A, Budker D and Walsworth R L 2013 Solid-state electronic spin coherence time approaching one second *Nat. Commun.* **4** 1743
[121] Bartling H P, Abobeih M H, Pingault B, Degen M J, Loenen S J H, Bradley C E, Randall J, Markham M, Twitchen D J and Taminiau T H 2022 Entanglement of spin-pair qubits with intrinsic dephasing times exceeding a minute *Phys. Rev. X* **12** 011048
[122] Baber S, Malein R N E, Khatri P, Keatley P S, Guo S, Withers F, Ramsay A J and Luxmoore I J 2022 Excited state spectroscopy of boron vacancy defects in hexagonal boron nitride using time-resolved optically detected magnetic resonance *Nano Lett.* **22** 461–7
[123] Haykal A *et al* 2022 Decoherence of V_B^- in defects in monoisotopic hexagonal boron nitride *Nat. Commun.* **13** 4347
[124] Reimers J R, Shen J, Kianinia M, Bradac C, Aharonovich I, Ford M J and Piecuch P 2020 Photoluminescence, photophysics and photochemistry of the V_B^- defect in hexagonal boron nitride *Phys. Rev. B* **102** 144105
[125] Mendelson N *et al* 2022 Coupling spin defects in a layered material to nanoscale plasmonic cavities *Adv. Mater.* **34** 2106046
[126] Xu X *et al* 2023 Greatly enhanced emission from spin defects in hexagonal boron nitride enabled by a low-loss plasmonic nanocavity *Nano Lett.* **23** 25–33
[127] Clua-Provost T *et al* 2024 Spin-dependent photodynamics of boron-vacancy centers in hexagonal boron nitride *Phys. Rev. B* **110** 014104
[128] Woodward J R 2002 Radical pairs in solution *Prog. React. Kinet. Mech.* **27** 165–207
[129] Whitefield B *et al* 2026 Narrowband quantum emitters in hexagonal boron nitride with optically addressable spins *Nat. Mater.* **25** 412–9
[130] Azuma K, Economou S E, Elkouss D, Hilaire P, Jiang L, Lo H K and Tzitrin I 2023 Quantum repeaters: from quantum networks to the quantum internet *Rev. Mod. Phys.* **95** 045006
[131] Childress L, Taylor J M, Sørensen A S and Lukin M D 2005 Fault-tolerant quantum repeaters with minimal physical resources and implementations based on single-photon emitters *Phys. Rev. A* **72** 052330
[132] Fang R-Z *et al* 2024 Experimental generation of spin-photon entanglement in silicon carbide *Phys. Rev. Lett.* **132** 160801
[133] Cholsuk C, Çakan A, Suwanna S and Vogl T 2024 Identifying electronic transitions of defects in hexagonal boron nitride for quantum memories *Adv. Opt. Mater.* **12** 2302760
[134] Wehner S, Elkouss D and Hanson R 2018 Quantum internet: a vision for the road ahead *Science* **362** 2302760

[135] McMahon P L and Greve K D 2015 Towards quantum repeaters with solid-state qubits: spin-photon entanglement generation using self-assembled quantum dots *Engineering the Atom-Photon Interaction: Controlling Fundamental Processes With Photons, Atoms and Solids* (Springer) pp 365–402
[136] Knaut C M *et al* 2024 Entanglement of nanophotonic quantum memory nodes in a telecom network *Nature* **629** 573–8
[137] Ye M, Seo H and Galli G 2019 Spin coherence in two-dimensional materials *npj Comput. Mater.* **5** 44
[138] Tárkányi A and Ivády V 2025 Understanding decoherence of the boron vacancy center in hexagonal boron nitride *Adv. Funct. Mater.* **36** e11300
[139] Itoh K M and Watanabe H 2014 Isotope engineering of silicon and diamond for quantum computing and sensing applications *MRS Commun.* **4** 143–57
[140] Viola L and Lloyd S 1998 Dynamical suppression of decoherence in two-state quantum systems *Phys. Rev. A* **58** 2733
[141] Rizzato R *et al* 2023 Extending the coherence of spin defects in hBN enables advanced qubit control and quantum sensing *Nat. Commun.* **14** 5089
[142] Seo H, Falk A L, Klimov P V, Miao K C, Galli G and Awschalom D D 2016 Quantum decoherence dynamics of divacancy spins in silicon carbide *Nat. Commun.* **7** 12935
[143] Murzakhanov F F *et al* 2022 Electron-nuclear coherent coupling and nuclear spin readout through optically polarized V_B^- spin states in hBN *Nano Lett.* **22** 2718–24
[144] Lee J, Park H and Seo H 2022 First-principles theory of extending the spin qubit coherence time in hexagonal boron nitride *npj 2D Mater. Appl.* **6** 60
[145] Wolfowicz G, Tyryshkin A M, George R E, Riemann H, Abrosimov N V, Becker P, Pohl H J, Thewalt M L W, Lyon S A and Morton J L 2013 Atomic clock transitions in silicon-based spin qubits *Nat. Nanotechnol.* **8** 561–4
[146] Neumann P, Mizuochi N, Rempp F, Hemmer P, Watanabe H, Yamasaki S, Jacques V, Gaebel T, Jelezko F and Wrachtrup J 2008 Multipartite entanglement among single spins in diamond *Science* **320** 1326–9
[147] Wei S H *et al* 2022 Towards real-world quantum networks: a review *Laser Photonics Rev.* **16** 2100219
[148] Aslam N, Zhou H, Urbach E K, Turner M J, Walsworth R L, Lukin M D and Park H 2023 Quantum sensors for biomedical applications *Nat. Rev. Phys.* **5** 157–69
[149] Rizzato R, von Grafenstein N R and Bucher D B 2023 Quantum sensors in diamonds for magnetic resonance spectroscopy: current applications and future prospects *Appl. Phys. Lett.* **123** 260502
[150] Rovny J, Gopalakrishnan S, Jayich J A C B, Maletinsky P, Demler E and de Leon N P 2024 Nanoscale diamond quantum sensors for many-body physics *Nat. Rev. Phys.* **6** 753–68
[151] Budker D and Romalis M 2007 Optical magnetometry *Nat. Phys.* **3** 227
[152] Balasubramanian G *et al* 2008 Nanoscale imaging magnetometry with diamond spins under ambient conditions *Nature* **455** 648
[153] Maze J R *et al* 2008 Nanoscale magnetic sensing with an individual electronic spin in diamond *Nature* **455** 644
[154] Rondin L, Tetienne J-P, Spinicelli P, Savio C D, Karrai K, Dantelle G, Thiaville A, Rohart S, Roch. J F and Jacques V 2012 Nanoscale magnetic field mapping with a single spin scanning probe magnetometer *Appl. Phys. Lett.* **100** 153118
[155] Rondin L, Tetienne J-P, Hingant T, Roch J F, Maletinsky P and Jacques V 2014 Magnetometry with nitrogen-vacancy defects in diamond *Rep. Prog. Phys.* **77** 056503
[156] Barry J F, Schloss J M, Bauch E, Turner M J, Hart C A, Pham L M and Walsworth R L 2020 Sensitivity optimization for NV-diamond magnetometry *Rev. Mod. Phys.* **92** 015004
[157] Healey A J *et al* 2023 Quantum microscopy with van der Waals heterostructures *Nat. Phys.* **19** 87–91
[158] Gao X, Vaidya S, Dikshit S, Ju P, Shen K, Jin Y, Zhang S and Li T 2024 Nanotube spin defects for omnidirectional magnetic field sensing *Nat. Commun.* **15** 7697
[159] Kavčič A, Podlipec R, Krišelj A, Jelen A, Vella D and Humar M 2024 Intracellular biocompatible hexagonal boron nitride quantum emitters as single-photon sources and barcodes *Nanoscale* **16** 4691–702
[160] Gottscholl A, Diez M, Soltamov V, Kasper C, Krauße D, Sperlich A, Kianinia M, Bradac C, Aharonovich I and Dyakonov V 2021 Spin defects in hBN as promising temperature, pressure and magnetic field quantum sensors *Nat. Commun.* **12** 4480
[161] Liu Z *et al* 2025 Temperature-dependent spin-phonon coupling of boron-vacancy centers in hexagonal boron nitride *Phys. Rev. B* **111** 024108
[162] He G *et al* 2025 Probing stress and magnetism at high pressures with two-dimensional quantum sensors *Nat. Commun.* **16** 8162
[163] Yang T, Mendelson N, Li C, Gottscholl A, Scott J, Kianinia M, Dyakonov V, Toth M and Aharonovich I 2022 Spin defects in hexagonal boron nitride for strain sensing on nanopillar arrays *Nanoscale* **14** 5239–44
[164] Lyu X, Tan Q, Wu L, Zhang C, Zhang Z, Mu Z, Zúñiga-Pérez J, Cai H and Gao W 2022 Strain quantum sensing with spin defects in hexagonal boron nitride *Nano Lett.* **22** 6553–9
[165] Kumar P *et al* 2022 Magnetic imaging with spin defects in hexagonal boron nitride *Phys. Rev. Appl.* **18** L061002
[166] Zhou J *et al* 2024 Sensing spin wave excitations by spin defects in few-layer-thick hexagonal boron nitride *Sci. Adv.* **10** 8495
[167] Huang M *et al* 2022 Wide field imaging of van der Waals ferromagnet Fe_3GeTe_2 by spin defects in hexagonal boron nitride *Nat. Commun.* **13** 5369
[168] Zang H-X *et al* 2025 Detecting and imaging of magnons at nanoscale with van der Waals quantum sensor *Adv. Funct. Mater.* **35** 2412166
[169] Mañas-Valero S, Doedes Y C, Bondarenko A, Borst M, Kurdi S, Poirier T, Edgar J H, Jacques V, Blanter Y M and van der Sar T 2025 Isofrequency spin-wave imaging using color center magnetometry for magnon spintronics *Nat. Commun.* **17** 379
[170] Zhou F, Jiang Z, Liang H, Ru S, Bettiol A A and Gao W 2023 DC magnetic field sensitivity optimization of spin defects in hexagonal boron nitride *Nano Lett.* **23** 6209–15
[171] Tang J, Yin Z, Hart C A, Blanchard J W, Oon J T, Bhalerao S, Schloss J M, Turner M J and Walsworth R L 2023 Quantum diamond microscope for dynamic imaging of magnetic fields *Adv. Quantum Sci.* **5** 044403
[172] Gong R, He G, Gao X, Ju P, Liu Z, Ye B, Henriksen E A, Li T and Zu C 2023 Coherent dynamics of strongly interacting electronic spin defects in hexagonal boron nitride *Nat. Commun.* **14** 3299
[173] Patrickson C J, Baber S, Gaál B B, Ramsay A J and Luxmoore I J 2024 High frequency magnetometry with an ensemble of spin qubits in hexagonal boron nitride *npj Quantum Inf.* **10** 5
[174] Patrickson C J, Haemmerli V, Guo S, Ramsay A J and Luxmoore I J 2025 Microwave quantum heterodyne sensing using a continuous concatenated dynamical decoupling protocol *Nat. Commun.* **16** 4380
[175] Udvarhelyi P, Clua-Provost T, Durand A, Li J, Edgar J H, Gil B, Cassabois G, Jacques V and Gali A 2023 A planar defect spin sensor in a two-dimensional material susceptible to strain and electric fields *npj Comput. Mater.* **9** 150
[176] Mu Z *et al* 2025 Magnetic imaging under high pressure with a spin-based quantum sensor integrated in a van der Waals heterostructure *Nat. Commun.* **16** 8574
[177] Dolde F *et al* 2011 Electric-field sensing using single diamond spins *Nat. Phys.* **7** 459–63
[178] Durand A *et al* 2023 Optically active spin defects in few-layer thick hexagonal boron nitride *Phys. Rev. Lett.* **131** 116902

[179] Sangtawesin S *et al* 2019 Origins of diamond surface noise probed by correlating single-spin measurements with surface spectroscopy *Phys. Rev. X* **9** 031052
[180] Tetienne J-P, Rondin L, Spinicelli P, Chipaux M, Debuisschert T, Roch J F and Jacques V 2012 Magnetic-field-dependent photodynamics of single NV defects in diamond: an application to qualitative all-optical magnetic imaging *New J. Phys.* **14** 103033
[181] Lee S Y *et al* 2013 Readout and control of a single nuclear spin with a metastable electron spin ancilla *Nat. Nanotechnol.* **8** 487–92
[182] Foglszinger J, Denisenko A, Kornher T, Schreck M, Knolle W, Yavkin B, Kolesov R and Wrachtrup J 2022 TR12 centers in diamond as a room temperature atomic scale vector magnetometer *npj Quantum Inf.* **8** 65
[183] Robertson I O, Johnson B C, Thalassinos G, Scholten S C, Rietwyk K J, Gibson B C, Tetienne J-P and Broadway D A 2025 Radiofrequency receiver based on isotropic solid-state spins *ACS Photonics* **12** 581–7
[184] Freysoldt C, Grabowski B, Hickel T, Neugebauer J, Kresse G, Janotti A and de Walle C G V 2014 First-principles calculations for point defects in solids *Rev. Mod. Phys.* **86** 253–305
[185] Ivády V, Abrikosov I A and Gali A 2018 First principles calculation of spin-related quantities for point defect qubit research *npj Comput. Mater.* **4** 1–13
[186] Gali A 2023 Recent advances in the ab initio theory of solid-state defect qubits *Nanophotonics* **12** 359–97
[187] Alkauskas A, Buckley B B, Awschalom D D and de Walle C G V 2014 First-principles theory of the luminescence lineshape for the triplet transition in diamond NV centres *New J. Phys.* **16** 073026
[188] Kobayashi R, Reimers J R, Sajid A and Ford M J 2019 Understanding and calibrating density-functional-theory calculations describing the energy and spectroscopy of defect sites in hexagonal boron nitride *J. Chem. Theory Comput.* **14** 1602–13
[189] Barcza G, Ivády V, Szilvási T, Vörös M, Veis L, Gali A and Legeza O 2021 Dmrg on top of plane-wave Kohn–Sham orbitals: a case study of defected boron nitride *J. Chem. Theory Comput.* **17** 1143–54
[190] Cholsuk C, Suwanna S and Vogl T 2023 Comprehensive scheme for identifying defects in solid-state quantum systems *J. Phys. Chem. Lett.* **14** 6564–71
[191] Benedek Z, Babar R, Ganyecz A, Szilvási T, Legeza O, Barcza G and Ivády V 2023 Symmetric carbon tetramers forming spin qubits in hexagonal boron nitride *npj Comput. Mater.* **9** 187
[192] Davidsson J 2020 Theoretical polarization of zero phonon lines in point defects *J. Phys.: Condens. Matter* **32** 385502
[193] Szász K, Hornos T, Marsman M and Gali A 2013 Hyperfine coupling of point defects in semiconductors by hybrid density functional calculations: the role of core spin polarization *Phys. Rev. B* **88** 075202
[194] Takács I and Ivády V 2024 Accurate hyperfine tensors for solid state quantum applications: case of the NV center in diamond *Commun. Phys.* **7** 1–6
[195] Hayee F *et al* 2020 Revealing multiple classes of stable quantum emitters in hexagonal boron nitride with correlated optical and electron microscopy *Nat. Mater.* **19** 534–9
[196] Singla S, Joshi P, López-Morales G I, Sarkar S, Flick J and Chakraborty B 2024 Probing correlation of optical emission and defect sites in hexagonal boron nitride by high-resolution STEM-EELS *Nano Lett.* **24** 9212–20
[197] Pelliciari J *et al* 2024 Elementary excitations of single-photon emitters in hexagonal boron nitride *Nat. Mater.* **23** 1230
[198] Murzakhanov F F, Yavkin B V, Mamin G V, Orlinskii S B, Mumdzhi I E, Gracheva I N, Gabbasov B F, Smirnov A N, Davydov V Y and Soltamov V A 2021 Creation of negatively charged boron vacancies in hexagonal boron nitride crystal by electron irradiation and mechanism of inhomogeneous broadening of boron vacancy-related spin resonance lines *Nanomaterials* **11** 1373
[199] Healey A J *et al* 2024 Optimisation of electron irradiation for creating spin ensembles in hexagonal boron nitride *Mater. Quantum Technol.* **4** 035701
[200] Kianinia M, White S, Fröch J E, Bradac C and Aharonovich I 2020 Generation of spin defects in hexagonal boron nitride *ACS Photonics* **7** 2147–52
[201] Guo N J *et al* 2022 Generation of spin defects by ion implantation in hexagonal boron nitride *ACS Omega* **7** 1733–9
[202] Gao X, Pandey S, Kianinia M, Ahn J, Ju P, Aharonovich I, Shivaram N and Li T 2021 Femtosecond laser writing of spin defects in hexagonal boron nitride *ACS Photonics* **8** 994–1000
[203] Yang Y-Z *et al* 2023 Laser direct writing of visible spin defects in hexagonal boron nitride for applications in spin-based technologies *ACS Appl. Nano Mater.* **6** 6407–14
[204] Sarkar S, Xu Y, Mathew S, Lal M, Chung J-Y, Lee H Y, Watanabe K, Taniguchi T, Venkatesan T and Gradečak S 2024 Identifying luminescent boron vacancies in h-bn generated using controlled He^+ ion irradiation *Nano Lett.* **24** 43–50
[205] Zabelotsky T *et al* 2023 Creation of boron vacancies in hexagonal boron nitride exfoliated from bulk crystals for quantum sensing *ACS Appl. Nano Mater.* **6** 21671–8
[206] Suzuki T, Yamazaki Y, Taniguchi T, Watanabe K, Nishiya Y, Matsushita Y-ichiro, Harii K, Masuyama Y, Hijikata Y and Ohshima T 2023 Spin property improvement of boron vacancy defect in hexagonal boron nitride by thermal treatment *Appl. Phys. Express* **16** 032006
[207] Liang H, Chen Y, Yang C, Watanabe K, Taniguchi T, Eda G and Bettiol A A 2023 High sensitivity spin defects in hBN created by high-energy he beam irradiation *Adv. Opt. Mater.* **11** 2201941
[208] Carbone A *et al* 2025 Quantifying the creation of negatively charged boron vacancies in he-ion irradiated hexagonal boron nitride *Phys. Rev. Mater.* **9** 056203
[209] Vlassiouk I V *et al* 2025 Defect engineering in large-scale CVD-grown hexagonal boron nitride: formation, spectroscopy and spin relaxation dynamics *Small* **22** e06874
[210] Clua-Provost T *et al* 2024 Impact of thickness-dependent nanophotonic effects on the optical response of color centers in hexagonal boron nitride *Nano Lett.* **24** 12915–20
[211] Fraunié J *et al* 2025 Charge state tuning of spin defects in hexagonal boron nitride *Nano Lett.* **25** 5836–42
[212] Khatri P, Ramsay A J, Malein R N E, Chong H M H and Luxmoore I J 2020 Optical gating of photoluminescence from color centers in hexagonal boron nitride *Nano Lett.* **20** 4256–63
[213] Jules F *et al* 2025 Non-radiative energy transfer between boron vacancies in hexagonal boron nitride and other 2D materials (arXiv:2512.03970 [cond-mat.mtrl-sci])
[214] Proscia N V, Shotan Z, Jayakumar H, Reddy P, Cohen C, Dollar M, Alkauskas A, Doherty M, Meriles C A and Menon V M 2018 Near-deterministic activation of room-temperature quantum emitters in hexagonal boron nitride *Optica* **5** 1128–34
[215] Ziegler J, Klaiss R, Blaikie A, Miller D, Horowitz V R and Alemán B J 2019 Deterministic quantum emitter formation in hexagonal boron nitride via controlled edge creation *Nano Lett.* **19** 2121–7